

Using Linearized Optimal Transport to Predict the Evolution of Stochastic Particle Systems

Nicholas Karris¹, Evangelos A. Nikitopoulos^{*2}, Ioannis G. Kevrekidis^{†3}, Seungjoon Lee⁴,
and Alexander Cloninger^{‡1}

¹University of California, San Diego

²University of Michigan

³Johns Hopkins University

⁴California State University, Long Beach

February 15, 2025

Abstract

We develop an Euler-type method to predict the evolution of a time-dependent probability measure without explicitly learning an operator that governs its evolution. We use linearized optimal transport theory to prove that the measure-valued analog of Euler’s method is first-order accurate when the measure evolves “smoothly.” In applications of interest, however, the measure is an empirical distribution of a system of stochastic particles whose behavior is only accessible through an agent-based micro-scale simulation. In such cases, this empirical measure does not evolve smoothly because the individual particles move chaotically on short time scales. However, we can still perform our Euler-type method, and when the particles’ collective distribution approximates a measure that *does* evolve smoothly, we observe that the algorithm still accurately predicts this collective behavior over relatively large Euler steps. We specifically demonstrate the efficacy of our approach by showing that our algorithm vastly reduces the number of micro-scale steps needed to correctly approximate long-term behavior in two illustrative examples, reflected Brownian motion and a model of bacterial chemotaxis.

Keyphrases: Optimal Transport, Wasserstein Manifold, Euler’s Method, Particle Simulation Speed-up, Fast-Slow Systems, Bacterial Chemotaxis

MSC (2020): 49Q22, 37M05, 65C35

*Supported by NSF grant DGE 2038238

†Partially supported by the US Department of Energy

‡Supported by NSF grants DMS 2012266 and CISE CCF 2403452

Contents

1	Introduction	2
1.1	Practical Utility for Agent-based Models	4
1.2	Major Contributions	6
2	Preliminaries	6
2.1	Optimal Transport Background	6
2.2	Tangent Fields and Linearized Optimal Transport	7
3	Euler-type Methods on the Wasserstein Manifold	9
3.1	Motivation from Euclidean Space	9
3.2	Euler’s Method on the Wasserstein Manifold	9
3.3	Euler’s Method with Imperfect Information	13
4	Euler-type Method for Empirical Measures of Particle Systems	14
4.1	Choosing an Appropriate Step Size	16
4.2	Additional Considerations	18
4.3	Detailed Description of Our Algorithm	19
5	Experiments with Reflected Brownian Motion	20
6	Experiments with Bacterial Chemotaxis	24
6.1	Problem Setup	25
6.2	Experimental Results	26
6.3	Computational Improvement	28
6.4	Comparison with Different Re-initializations	28
	Acknowledgments	31
	References	31

1 Introduction

In this paper, we consider the problem of predicting the evolution of a time-dependent probability measure $t \mapsto \mu_t$ on \mathbb{R}^d , representing the distribution of particles in some physical system, given very limited information about the system’s underlying dynamics. Often, the physics governing the system can be approximated by an “oracle operator” E_h that takes as input the present state μ_t of the system and returns an approximation $E_h(\mu_t) \approx \mu_{t+h}$ after “evolving” according to the underlying dynamics for a short time h . As an example, E_h could be represented by an agent-based micro-scale model, in which individual particles act autonomously but exhibit some collective behavior when viewed as a group.

A natural way to understand such physical systems is to attempt to learn the oracle operator E_h . Many approaches to learning operators focus on tracking a sample of μ_t through the actions of E_h and then interpolating the results [20, 12, 13, 22, 17]. However, in many applications, it is not possible to track the action of E_h on individual sample particles. We consider a different perspective on tackling this problem. Instead of learning the entire operator E_h , we ask whether it is possible to predict the measure’s evolution *without* needing to understand the underlying dynamics. Explicitly, given μ_t and $E_h(\mu_t) \approx \mu_{t+h}$ for only some small time step h , can we predict the measure μ_{t+H} for a larger time step H ? If so, then we can build an Euler-type method for approximating the long-term evolution of the distribution by making successive approximations. There are several potential approaches to this problem, each with its own merits and drawbacks. One drawback common to

most approaches, though, is a reliance on computing and predicting summary statistics and then reconstructing a distribution with the predicted statistics. We avoid this reliance on summary statistics and instead take a linearized optimal transport (LOT)-based approach informed by the geometry of the Wasserstein manifold that directly uses the measure-valued data to predict μ_{t+H} .

To explain the philosophy of our prediction algorithm, we briefly discuss curves on the Wasserstein manifold. Precise definitions and results are reviewed in Section 2. Let $\mathcal{P}_2(\mathbb{R}^d)$ be the space of Borel probability measures on \mathbb{R}^d with finite second moment, and let W_2 be the (2-)Wasserstein distance on $\mathcal{P}_2(\mathbb{R}^d)$. If μ is a sufficiently “smooth” curve, written $t \mapsto \mu_t$, on the “Wasserstein manifold” $\mathbb{W}_2 := (\mathcal{P}_2(\mathbb{R}^d), W_2)$, then there exists a “tangent field” governing its evolution. Explicitly, there is a time-dependent vector field $\mathbf{v}_t: \mathbb{R}^d \rightarrow \mathbb{R}^d$ representing the time derivative of μ through the continuity equation

$$\partial_t \mu_t + \nabla \cdot (\mathbf{v}_t \mu_t) = 0.$$

Intuitively speaking, the vector field \mathbf{v}_t describes the “flow of mass” of the evolving measure. Furthermore, if μ always has a density, then its tangent field can be computed using optimal transport maps:

$$\mathbf{v}_t = \lim_{h \rightarrow 0} \frac{T_{\mu_t}^{\mu_{t+h}} - \text{id}}{h},$$

where $T_{\mu_t}^{\mu_{t+h}}$ is the optimal transport map from μ_t to μ_{t+h} and $\text{id} = \text{id}_{\mathbb{R}^d}$. This leads to the key insight that one can use optimal transport maps from μ_t to μ_{t+h} for small values of h to understand approximately where each infinitesimal piece of mass of μ_t is moving. Moreover, the interpretation of $t \mapsto \mathbf{v}_t$ as the tangent field to the curve μ on the Wasserstein manifold suggests that the “geodesic starting at μ_t in the direction of \mathbf{v}_t ,” given by $s \mapsto (s\mathbf{v}_t + \text{id})_{\#} \mu_t$, is a first-order accurate approximation of the true curve. This result is made precise in Theorem 2.6(iii). It also suggests a measure-valued analog of Euler’s method for ODEs on the Wasserstein manifold, which we develop in Section 3.2.

Euler’s method requires complete knowledge of the dynamics of an ODE. As discussed in the first paragraph, we suppose instead that we can only access dynamics information by querying an oracle E_h for a short time h . In this case, although we cannot know the true tangent field $t \mapsto \mathbf{v}_t$, we can hope to approximate it by

$$\mathbf{v}_t^h := \frac{T_{\mu_t}^{E_h(\mu_t)} - \text{id}}{h} \approx \frac{T_{\mu_t}^{\mu_{t+h}} - \text{id}}{h}.$$

We then use this approximate tangent field to approximate μ_{t+H} as $\tilde{\mu}_{t+H} := (H\mathbf{v}_t^h + \text{id})_{\#} \mu_t$, the geodesic starting at μ_t in the direction \mathbf{v}_t^h evaluated at time H . Iterating such approximations leads to an Euler’s method “with incomplete information,” which we discuss in Sections 3.1 and 3.3 for sufficiently “smooth” curves with densities at all times. Note well that this Euler-type method allows us to predict the evolution of μ without attempting to learn anything about the operator E_h .

A key feature of the above-described approach is that Euler’s method with incomplete information can be formulated in fairly arbitrary situations, e.g., for chaotically evolving discrete measures. In this paper, we specifically consider cases arising from particle systems. Let $x_1(t), \dots, x_N(t)$ be a system of N (random) particles in \mathbb{R}^d evolving in time, and define $\mu_t^N := N^{-1} \sum_{i=1}^N \delta_{x_i(t)}$. If $\nu := \mu_t^N$ and $\rho := E_h(\mu_t^N) \approx \mu_{t+h}^N$, then the Euler-type method described above becomes the following algorithm:

1. Compute a (discrete) optimal transport plan from ν to ρ , and compute the barycentric projection to obtain a map T .
2. Use the map from Step 1 to form the difference quotient $\mathbf{v}_t^h := \frac{T - \text{id}}{h}$.
3. For each point in the support of ν , take an Euler step using its current location and the velocity given by the “optimal transport vector field” \mathbf{v}_t^h .
4. Set $\tilde{\mu}_{t+H}^N$ to be the uniform distribution on the points obtained by performing the Euler step from Step 3 on each point in the support of ν .
5. Repeat Steps 1–4 using $\tilde{\mu}_{t+H}^N$ as the “initial measure” ν .

Our actual algorithm, laid out in Section 4.3, is more complicated. Steps 1–5 above suffice for the present introductory discussion.

It is important to highlight that *both* regularity properties demanded of μ in the earlier discussion of tangent fields and Euler-type methods are generally false for μ^N , the curve $t \mapsto \mu_t^N$. Certainly, μ^N never has a density because it is always a discrete measure. Moreover, μ^N can fail to be “smooth” because the particles may evolve chaotically. For example, if x_1, \dots, x_N are Brownian motions, then the sample paths are nowhere differentiable. Therefore, a priori, it is not clear the algorithm above actually works in this setting. In many systems of interest, however, there is a “smooth” curve $t \mapsto \mu_t$ of measures with densities such that “ $\mu^N \approx \mu$ ” for large N , e.g., if we start with the curve μ and the x_i ’s are i.i.d. samples of μ . For certain such systems (Sections 5 and 6), we experimentally demonstrate that the LOT-based algorithm described above can be used to predict the evolution of the particle distribution μ^N without explicitly reconstructing the underlying distribution μ or learning the underlying dynamics described by E_h .

One application for which our approximation algorithm is particularly useful is if E_h is given by a computationally expensive micro-scale particle simulation, as it is in Section 6. Then we can think of μ_t^N as the locations of the particles at time t and $E_h(\mu_t^N) \approx \mu_{t+h}^N$ as their locations at the “next time step” in the simulation. The benefit of accurately predicting μ_{t+H}^N for a substantial time step $H \gg h$ is that one can then skip potentially many micro-scale steps in the simulation and still understand how μ^N evolves in time. Indeed, after predicting μ_{t+H}^N , one can reinitialize the simulation with particles at those locations, take another small step in the simulation to obtain an estimate for μ_{t+H+h}^N , and use the prediction algorithm again to approximate μ_{t+2H}^N . Following strategies of some projective integration techniques [8, 9, 27], doing this successively gives an Euler-type method for approximating the system’s behavior for a long time without the need to perform as many micro-scale steps. If the simulation is computationally expensive or if many particles and small time steps are required to observe long-term behavior, then having a way to reduce the number of micro-scale time steps could and, in Section 6, does yield significant computational speed improvements.

1.1 Practical Utility for Agent-based Models

To highlight the practical utility of our proposed algorithm, we consider agent-based micro-scale models of particle systems, specifically of so-called “fast-slow” systems. Such systems are difficult to analyze because each particle has multiple underlying variables impacting its behavior that update on vastly different time scales. In general, the “fast dynamics” update on short time

scales and generally manifest as chaotic short-time particle behavior. For example, a particle may quickly change directions many times as a result of its interactions with nearby particles. “Slow dynamics,” on the other hand, update on much longer time scales and generally manifest as the eventual emergence of a collective behavior of the particles, e.g., the migration of bacteria toward a higher concentration of a food source. Nominally, this means that in order to simulate such a system, a micro-scale simulation must be run with small time steps to capture the fast dynamics accurately, and *many* such time steps are required for the slow dynamics to emerge. Of course, this can be impractical when each step is computationally expensive.

Many approaches to understanding and more efficiently simulating these types of systems have been explored. A few examples of so-called “multi-scale methods” are presented in [16, 15, 10, 29, 6, 5], and other “projective integration methods” are proposed in [8, 7] and others. The techniques of Neural ODEs and Continuous Normalizing Flows can also be used to understand similar problems, e.g., in [14, 28]. Each of these techniques avoids the computational cost of simulating the system, but they all do so by restricting attention to specific classes of particle systems. In contrast, the method we propose assumes essentially nothing about the particular class of the underlying micro-scale simulator, only that the bulk behavior appears “smooth.” In particular, it does not require an assumption about the precise form of the dynamics of an agent-based model, nor does it attempt to learn those dynamics explicitly. We avoid the computational cost not by making an assumption about the problem but by using optimal transport to detect the slow dynamics after only a small number of micro-scale steps. The key insight is that, for systems that exhibit this multi-scale behavior, we can use an optimal transport map to effectively ignore the chaotic motion of *individual* particles in favor of focusing on the slower collective behavior.

This insight has been used to a similar effect before: [27] explores how a micro-scale model of bacterial chemotaxis in 1-D could be sped up by computing Euler-type steps after first sorting the locations of the bacteria. In one dimension, sorting a discrete distribution is exactly the same as computing an optimal transport map, so it turns out that their approach is similar to ours. This observation was the genesis of the present paper. To demonstrate the practical utility of our algorithm, we perform a similar experiment with the same chemotaxis model (Section 6). We show that our algorithm enables us to skip many micro-scale steps and still approximate the long-term behavior of the bacteria distribution. Compared to only running the micro-scale simulation, this cuts the computation time roughly in half without substantially sacrificing accuracy.

Framing the algorithm in terms of optimal transport as opposed to particle sorting not only provides it theoretical motivation, as discussed earlier, but also enables its immediate generalization to particle systems in higher dimensions. To demonstrate its efficacy on 2-D particle systems, we use the algorithm to simulate 2-D reflected Brownian motion in a rectangle (Section 5). While standard micro-scale models of Brownian motion are computationally cheap — so our algorithm provides less practical benefit in the form of speeding up simulations — the example is a good proof of concept for higher dimensions because it exhibits multi-scale behavior as described above. Specifically, the particles move chaotically on short time scales, yet the overall distribution evolves slowly and predictably.

1.2 Major Contributions

- We use linearized optimal transport to describe an analog of Euler’s method for differential equations on the Wasserstein manifold (Section 3.2).
- We prove that, under sufficient regularity conditions, our measure-valued Euler’s method with step size H has local truncation error $\mathcal{O}(H^2)$ and corresponding global error $\mathcal{O}(H)$ (Theorems 3.3 and 3.9).
- We detail an algorithm that uses linearized optimal transport to approximate the evolution of discrete particle systems (Section 4).
- We demonstrate the efficacy of our algorithm and illustrate the necessity of using optimal transport in place of particle-wise methods (Section 5).
- We apply our approximation algorithm to bacterial chemotaxis as described in [27] and discuss its computational benefits (Section 6).

2 Preliminaries

2.1 Optimal Transport Background

Let $\mathcal{P}(\mathbb{R}^d)$ be the set of Borel probability measures on \mathbb{R}^d , and let $\mathcal{P}_2(\mathbb{R}^d)$ be the set of measures $\mu \in \mathcal{P}(\mathbb{R}^d)$ such that $\int_{\mathbb{R}^d} \|x\|_2^2 d\mu(x) < \infty$. For a measurable function $T : \mathbb{R}^d \rightarrow \mathbb{R}^d$ and a measure $\sigma \in \mathcal{P}(\mathbb{R}^d)$, the pushforward of σ by T is the measure $T_{\#}\sigma$ defined by

$$(T_{\#}\sigma)(A) := \sigma(T^{-1}(A))$$

where $A \subset \mathbb{R}^d$ is measurable and $T^{-1}(A)$ is the preimage of A under T .

Given $\sigma, \mu \in \mathcal{P}_2(\mathbb{R}^d)$, a classical problem is to seek a map T transporting σ to μ in the sense that $T_{\#}\sigma = \mu$. Below is a fundamental result in optimal transport theory that provides the existence and uniqueness of “optimal” such T .

Theorem 2.1 (Brenier [3]). *Let $\sigma, \mu \in \mathcal{P}_2(\mathbb{R}^d)$, and suppose σ has a density with respect to the Lebesgue measure \mathcal{L}^d . There exists a σ -a.e. unique map $T : \mathbb{R}^d \rightarrow \mathbb{R}^d$ that solves the optimization problem*

$$\inf_{\{S: S_{\#}\sigma = \mu\}} \int_{\mathbb{R}^d} \|x - S(x)\|_2^2 d\sigma(x). \quad (2.2)$$

Moreover, there exists a convex function $\phi : \mathbb{R}^d \rightarrow \mathbb{R}$, σ -a.e. unique up to an additive constant, such that $T = \nabla\phi$.

Definition 2.3. *The map T given in Theorem 2.1 is the optimal transport map from σ to μ , and we denote it T_{σ}^{μ} . The square root of the number in (2.2) is the (2-)Wasserstein distance between σ and μ and is denoted by $W_2(\sigma, \mu)$, i.e.,*

$$W_2(\sigma, \mu) = \left(\inf_{\{S: S_{\#}\sigma = \mu\}} \int_{\mathbb{R}^d} \|x - S(x)\|_2^2 d\sigma(x) \right)^{\frac{1}{2}}.$$

It is well known that W_2 defines a metric on $\mathcal{P}_2(\mathbb{R}^d)$ (see, e.g., [25]).

Optimal transport is also possible between discrete measures. In general, this requires solving a more general optimization problem (the Kantorovich relaxation), but the following result guarantees that (2.2) is solvable in the case of uniform measures on the same finite number of points.

Proposition 2.4 (Proposition 2.1 in [25]). *If $\sigma = \frac{1}{N} \sum_{i=1}^N \delta_{x_i}$ and $\mu = \frac{1}{N} \sum_{i=1}^N \delta_{y_i}$ are uniform measures on the same number of points, then there exists an optimal transport map T_σ^μ that solves (2.2) (and also the Kantorovich relaxation). Moreover, if T_σ^μ is such a map, then there exists a permutation $\tau \in S_N$ such that $T_\sigma^\mu(x_i) = y_{\tau(i)}$ for all $i = 1, \dots, N$.*

Unlike in Theorem 2.1, optimal transport maps as in Proposition 2.4 are not necessarily unique, even σ -a.e. In this discrete case, the notation T_σ^μ will denote a particular choice of an optimal map.

2.2 Tangent Fields and Linearized Optimal Transport

As Otto first observed in [24], $\mathcal{P}_2(\mathbb{R}^d)$ has a formal infinite-dimensional Riemannian manifold structure. Because of this, the language and philosophy of differential geometry are often used in optimal transport theory and its applications. The key examples of interest to us and, more generally, the subject of linearized optimal transport (LOT) are the descriptions of the “tangent space(s)” and “exponential map” of the “Wasserstein manifold.” Below, we present the precise definition of the tangent space and a result that justifies its definition and underlies the philosophy and results of the present paper.

Definition 2.5. *For $\sigma \in \mathcal{P}_2(\mathbb{R}^d)$, define the tangent space $T_\sigma \mathbb{W}_2$ of the “Wasserstein manifold” $\mathbb{W}_2 := (\mathcal{P}_2(\mathbb{R}^d), W_2)$ at σ to be the closure in $L^2(\mathbb{R}^d, \sigma; \mathbb{R}^d)$ of $\{\nabla \phi : \phi \in C_c^\infty(\mathbb{R}^d)\}$.*

Theorem 2.6 (Theorem 8.3.1, Proposition 8.4.5, and Proposition 8.4.6 in [2]). *Let $I \subseteq \mathbb{R}$ be an open interval, let $\mu : I \rightarrow \mathcal{P}_2(\mathbb{R}^d)$ be an absolutely continuous curve in \mathbb{W}_2 (written $t \mapsto \mu_t$), and let $|\mu'|$ be the metric derivative of μ .*

- (i) *There exists a Borel vector field $I \times \mathbb{R}^d \ni (t, x) \mapsto \mathbf{v}(t, x) = \mathbf{v}_t(x) \in \mathbb{R}^d$ such that*

$$\|\mathbf{v}_t\|_{L^2(\mu_t)} := \left(\int_{\mathbb{R}^d} \|\mathbf{v}_t(x)\|_2^2 d\mu_t(x) \right)^{\frac{1}{2}} \leq |\mu'|_t \quad \text{for } \mathcal{L}^1\text{-a.e. } t \in I \quad (2.7)$$

and the continuity equation

$$\partial_t \mu_t + \nabla \cdot (\mathbf{v}_t \mu_t) = 0 \quad (2.8)$$

holds in the sense of distributions, i.e.,

$$\int_I \int_{\mathbb{R}^d} [\partial_t \phi(x, t) + \langle \mathbf{v}_t(x), \nabla_x \phi(x, t) \rangle] d\mu_t(x) dt = 0 \quad \text{for all } \phi \in C_c^\infty(\mathbb{R}^d \times I). \quad (2.9)$$

The map $t \mapsto \mathbf{v}_t$ is \mathcal{L}^1 -a.e. uniquely determined by (2.7) and (2.8) and is called the tangent field of μ .

- (ii) *If $\mathbf{v} : I \times \mathbb{R}^d \rightarrow \mathbb{R}^d$ is any Borel vector field satisfying (2.8), then (2.7) is satisfied if and only if $\mathbf{v}_t \in T_{\mu_t} \mathbb{W}_2$ for \mathcal{L}^1 -a.e. $t \in I$.*

(iii) If \mathbf{v} is the tangent field of μ , then

$$\lim_{h \rightarrow 0} \frac{W_2(\mu_{t+h}, (\text{id} + h\mathbf{v}_t)_\# \mu_t)}{|h|} = 0 \quad \text{for } \mathcal{L}^1\text{-a.e. } t \in I. \quad (2.10)$$

In particular, if $\mu_t \ll \mathcal{L}^d$ for all $t \in I$, then for \mathcal{L}^1 -a.e. $t \in I$,

$$\lim_{h \rightarrow 0} \frac{1}{h} (T_{\mu_t}^{\mu_{t+h}} - \text{id}) = \mathbf{v}_t \quad \text{in } L^2(\mathbb{R}^d, \mu_t; \mathbb{R}^d), \quad (2.11)$$

where $T_{\mu_t}^{\mu_{t+h}}$ is the optimal transport map from μ_t to μ_{t+h} .

Remark 2.12. For a general choice of $\sigma \in \mathcal{P}_2(\mathbb{R}^d)$, the best one can hope for is that the map $t \mapsto T_{\sigma}^{\mu_t} \in L^2(\mathbb{R}^d, \sigma; \mathbb{R}^d)$ is at most $\frac{1}{2}$ -Hölder continuous, even if the curve μ is Lipschitz [11, 21]. However, (2.11) says that by fixing t and choosing $\sigma = \mu_t$, the curve $h \mapsto T_{\mu_t}^{\mu_{t+h}}$ becomes “differentiable” at $h = 0$.

The exponential map can now be computed by finding the tangent field of a geodesic between two points $\mu_0, \mu_1 \in \mathcal{P}_2(\mathbb{R}^d)$. One can show (Section 7.2 of [2]) that if $T_{\mu_0}^{\mu_1}$ is an optimal transport map from μ_0 to μ_1 , then the curve

$$t \mapsto \mu_t := ((1-t)\text{id} + tT_{\mu_0}^{\mu_1})_\# \mu_0$$

is a (constant-speed) geodesic in W_2 from μ_0 to μ_1 . Furthermore, the vector field

$$\mathbf{v}_t(x) := (T_{\mu_0}^{\mu_1} - \text{id}) \left(((1-t)\text{id} + tT_{\mu_0}^{\mu_1})^{-1}(x) \right)$$

is the tangent field of the geodesic μ (Section 5.4 of [26]). Therefore, $\mathbf{v}_0 = T_{\mu_0}^{\mu_1} - \text{id}$ is the “tangent vector” to μ at $t = 0$. We conclude that the logarithm map, i.e., the inverse of the exponential map, at μ_0 is the map

$$\log_{\mu_0}^{\mathbb{W}_2} : \mathbb{W}_2 \rightarrow T_{\mu_0} \mathbb{W}_2, \quad \log_{\mu_0}^{\mathbb{W}_2}(\mu_1) = \mathbf{v}_0 = T_{\mu_0}^{\mu_1} - \text{id}.$$

Since $(\mathbf{v}_0 + \text{id})_\# \mu_0 = (T_{\mu_0}^{\mu_1})_\# \mu_0 = \mu_1$, it follows that the exponential map at μ_0 is the map

$$\exp_{\mu_0}^{\mathbb{W}_2} : T_{\mu_0} \mathbb{W}_2 \rightarrow \mathbb{W}_2, \quad \exp_{\mu_0}^{\mathbb{W}_2}(\mathbf{v}) = (\mathbf{v} + \text{id})_\# \mu_0.$$

(Please see [1, 19] for additional discussion.) In particular, if μ is a general absolutely continuous curve with velocity field \mathbf{v} , then Theorem 2.6(iii) says

$$\mu_{t+h} \approx (\text{id} + h\mathbf{v}_t)_\# \mu_t = \exp_{\mu_t}^{\mathbb{W}_2}(h\mathbf{v}_t)$$

for small h , which makes sense from a differential geometric point of view.

An important consequence of the previous paragraph’s description of the Wasserstein manifold’s logarithm map is that $\mu_1 \mapsto T_{\mu_0}^{\mu_1} - \text{id}$ “linearizes” $\mathcal{P}_2(\mathbb{R}^d)$; hence the L in LOT. Specifically, for a fixed reference measure $\sigma \in \mathcal{P}_2(\mathbb{R}^d)$, we can use the map $\mu \mapsto T_{\sigma}^{\mu} - \text{id}$ to “embed” the space $\mathcal{P}_2(\mathbb{R}^d)$ into the linear space $L^2(\mathbb{R}^d, \sigma; \mathbb{R}^d)$. There are many advantages to this linear embedding; see, for example, [30, 23] for computational speed-up and supervised learning and [4] for performing PCA.

3 Euler-type Methods on the Wasserstein Manifold

3.1 Motivation from Euclidean Space

In the sections following this one, we develop Euler-type methods for approximating the solutions to (nice) “ODEs” in the Wasserstein manifold. To understand these methods, it is helpful to discuss their analogs in the context of ODEs in \mathbb{R}^d . To this end, suppose we have a particle whose location at time t is described by some curve $\gamma(t)$ solving the IVP

$$\gamma(0) = x_0, \quad \gamma'(t) = f(t, \gamma(t)).$$

Our goal is to estimate $\gamma(T)$ for some large T . If we happen to have access to the underlying “dynamics” function f , then we can use ordinary Euler’s method: For a time step $H > 0$ and discrete times $t_n = nH$, approximate $\gamma(t_n) \approx \gamma_{(n)}$, where $\gamma_{(n)}$ is defined recursively by

$$\gamma_{(0)} = x_0, \quad \gamma_{(n+1)} = \gamma_{(n)} + Hf(t_n, \gamma_{(n)}) = \exp_{\gamma_{(n)}}^{\mathbb{R}^d}(Hf(t_n, \gamma_{(n)})),$$

where $\exp_{\gamma_{(n)}}^{\mathbb{R}^d}$ denotes the exponential map of \mathbb{R}^d at $\gamma_{(n)}$. Under sufficient regularity conditions on f , it is well known that Euler’s method is first-order accurate. The measure-valued analog of this method is developed in Section 3.2, and we prove an analogous accuracy result.

Suppose now that we have “imperfect information” about our system’s dynamics, i.e., that we do not have explicit access to the underlying function f . Then we cannot perform Euler’s method exactly. Instead, suppose we have access to some oracle E_h that, given a time t and a particle location γ , returns an approximation of where that particle would be at time $t + h$ for some small time step $h > 0$. (For us, this oracle will be a micro-scale numerical simulation that is only accurate for very small time steps h and is computationally expensive, so using it to simulate long-term behavior is impractical.) Given this information, we attempt to approximate $f(t, \gamma)$ by

$$f(t, \gamma) \approx \frac{E_h(t, \gamma) - \gamma}{h} =: \hat{f}(t, \gamma).$$

Using this approximation, we then define the Euler-type method

$$\gamma_{(0)} = x_0, \quad \gamma_{(n+1)} = \gamma_{(n)} + H\hat{f}(t_n, \gamma_{(n)}) = \exp_{\gamma_{(n)}}^{\mathbb{R}^d}(H\hat{f}(t_n, \gamma_{(n)})).$$

Of course, this method also makes sense for other approximations \hat{f} of f , and the error of the method depends on how well \hat{f} approximates f . While precise statements can be made, we omit the details for brevity. The measure-valued analog of this Euler-type method with a finite-difference approximation of the “dynamics” function is discussed in Section 3.3. In Section 4, we describe the “discrete case” of this approximation algorithm (in which E_h is a given micro-scale simulator).

3.2 Euler’s Method on the Wasserstein Manifold

According to Theorem 2.6’s characterization of tangent fields to curves on \mathbb{W}_2 , the measure-valued analog of the ODE $\gamma'(t) = f(t, \gamma(t))$ is the continuity equation

$$\partial_t \mu_t + \nabla \cdot (F(t, \mu_t) \mu_t) = 0, \tag{3.1}$$

where F is some “(time-dependent) vector field on the Wasserstein manifold.” Given such a “vector field” F and an initial measure μ_0 , the measure-valued analog of Euler’s method is the following: For discrete times $t_n = nH$, set

$$\mu_{(0)} := \mu_0, \quad \mu_{(n+1)} := \exp_{\mu_{(n)}}^{\mathbb{W}_2}(HF(t_n, \mu_{(n)})) = (\text{id} + HF(t_n, \mu_{(n)}))_{\#}\mu_{(n)}. \quad (3.2)$$

With this definition, one should expect that $\mu_{(n)} \approx \mu_{t_n}$ is first-order accurate under appropriate assumptions on F . The following result makes this precise.

Theorem 3.3. *Let $F : [0, T] \times \mathcal{P}_2(\mathbb{R}^d) \rightarrow (\mathbb{R}^d)^{\mathbb{R}^d} = \{\text{functions } \mathbb{R}^d \rightarrow \mathbb{R}^d\}$ be a map such that $F(t, \mu) \in T_{\mu}\mathbb{W}_2$ for all $t \in [0, T]$ and $\mu \in \mathcal{P}_2(\mathbb{R}^d)$. Suppose F satisfies the following Lipschitz conditions: There exist $L_1, L_2 \geq 0$ such that for all $t \in [0, T]$, $x_1, x_2 \in \mathbb{R}^d$, and $\mu_1, \mu_2 \in \mathcal{P}_2(\mathbb{R}^d)$,*

$$\|F(t, \mu)(x_1) - F(t, \mu)(x_2)\|_2 \leq L_1\|x_1 - x_2\|_2 \quad \text{and}$$

$$\|F(t, \mu_1) - F(t, \mu_2)\|_{L^2(\mu_i)} \leq L_2W_2(\mu_1, \mu_2) \quad (i = 1, 2).$$

If $\mu : [0, T] \rightarrow \mathcal{P}_2(\mathbb{R}^d)$ is an absolutely continuous curve solving the continuity equation (3.1) on $(0, T)$ in the sense of distributions and the function $(t, x) \mapsto \mathbf{v}_t(x) := F(t, \mu_t)(x)$ is (jointly) C^1 , then for μ_0 -a.e. $x \in \mathbb{R}^d$, the characteristic ODE

$$\gamma_x(0) = x, \quad \frac{d}{dt}\gamma_x(t) = \mathbf{v}_t(\gamma_x(t))$$

admits a unique C^2 solution. Furthermore, if

$$M := \left(\int_{\mathbb{R}^d} \max_{r \in [0, T]} \|\gamma_x''(r)\|_2^2 d\mu_0(x) \right)^{\frac{1}{2}} < \infty,$$

then for a time step $H > 0$ and discrete times $t_n := nH$, the sequence of Euler approximations iteratively defined by

$$\mu_{(0)} := \mu_0, \quad \mu_{(n+1)} := (\text{id} + HF(t_n, \mu_{(n)}))_{\#}\mu_{(n)}$$

satisfies

$$W_2(\mu_{(n)}, \mu_{t_n}) \leq \frac{HM}{2(L_1 + L_2)} \left(e^{nH(L_1 + L_2)} - 1 \right)$$

for all n such that $t_n = nH \leq T$.

The rest of this section is devoted to proving this result. To begin, observe that (2.10) says the local truncation error of Euler’s method on the Wasserstein manifold is $o(H)$. We now show that under our regularity assumptions on F , this method has local truncation error $\mathcal{O}(H^2)$. This is the same as the local truncation error of Euler’s method for curves in Euclidean space with bounded second derivative.

Lemma 3.4 (Proposition 8.1.8 in [2]). *Suppose $\mu : [0, T] \rightarrow \mathcal{P}_2(\mathbb{R}^d)$ is an absolutely continuous curve satisfying (2.8) on $(0, T)$ with velocity field \mathbf{v} satisfying*

$$\int_0^T \int_{\mathbb{R}^d} \|\mathbf{v}_t(x)\|_2 d\mu_t(x) dt < \infty \quad (3.5)$$

and

$$\int_0^T \left(\sup_{x \in B} \|\mathbf{v}_t(x)\|_2 + \text{Lip}(\mathbf{v}_t, B) \right) dt < \infty \quad (3.6)$$

for all compact set $B \subset \mathbb{R}^d$. Then for μ_0 -a.e. $x \in \mathbb{R}^d$, the ODE

$$\gamma_x(0) = x, \quad \frac{d}{dt} \gamma_x(t) = \mathbf{v}_t(\gamma_x(t)) \quad (3.7)$$

admits a globally defined solution, and

$$\mu_t = (T_t)_\# \mu_0 \quad \text{for all } t \in [0, T], \quad (3.8)$$

where $T_t(x) := \gamma_x(t)$.

Theorem 3.9. Assume the hypotheses of Lemma 3.4. Fix $t \in [0, T]$, let $H > 0$ be such that $t + H \leq T$, and let $\gamma_x : [t, t + H] \rightarrow \mathbb{R}^d$ be the solution to

$$\gamma_x(t) = x, \quad \gamma'_x(s) = \frac{d}{ds} \gamma_x(s) = \mathbf{v}_s(\gamma_x(s))$$

If γ_x is C^2 for μ_t -a.e. $x \in \mathbb{R}^d$ and

$$\int_{\mathbb{R}^d} \max_{r \in [t, t+H]} \|\gamma''_x(r)\|_2^2 d\mu_t(x) < \infty,$$

then

$$W_2(\mu_{t+H}, (\text{id} + H\mathbf{v}_t)_\# \mu_t) \leq \frac{H^2}{2} \left(\int_{\mathbb{R}^d} \max_{r \in [t, t+H]} \|\gamma''_x(r)\|_2^2 d\mu_t(x) \right)^{\frac{1}{2}}.$$

Proof. Define $T_s : \mathbb{R}^d \rightarrow \mathbb{R}^d$ by $T_s(x) = \gamma_x(s)$. By Lemma 3.4, $\mu_{t+H} = (T_{t+H})_\# \mu_t$, so

$$\begin{aligned} W_2^2(\mu_{t+H}, (\text{id} + H\mathbf{v}_t)_\# \mu_t) &\leq \int_{\mathbb{R}^d} \|T_{t+H}(x) - (\text{id} + H\mathbf{v}_t)(x)\|_2^2 d\mu_t(x) \\ &= \int_{\mathbb{R}^d} \|\gamma_x(t+H) - [x + H\mathbf{v}_t(x)]\|_2^2 d\mu_t(x). \end{aligned}$$

If γ_x is C^2 for a particular $x \in \mathbb{R}^d$, then

$$\begin{aligned} \gamma_x(t+H) &= \gamma_x(t) + H\gamma'_x(t) + \int_t^{t+H} \int_t^s \gamma''(r) dr ds \\ &= x + H\mathbf{v}_t(x) + \int_t^{t+H} \int_t^s \gamma''(r) dr ds. \end{aligned}$$

Hence, if γ_x is C^2 for μ_t -a.e. $x \in \mathbb{R}^d$, then

$$\begin{aligned} W_2^2(\mu_{t+H}, (\text{id} + H\mathbf{v}_t)_\# \mu_t) &\leq \int_{\mathbb{R}^d} \left\| \int_t^{t+H} \int_t^s \gamma''_x(r) dr ds \right\|_2^2 d\mu_t(x) \\ &\leq \int_{\mathbb{R}^d} \frac{H^4}{4} \max_{r \in [t, t+H]} \|\gamma''_x(r)\|_2^2 d\mu_t(x). \quad \square \end{aligned}$$

As in the Euclidean case, the fact that the local truncation error of Euler's method on the Wasserstein manifold is $\mathcal{O}(H^2)$ implies that, under our Lipschitz conditions on F , the global error is first order. This is exactly the content of Theorem 3.3.

Proof of Theorem 3.3. We first prove that the ODE (3.7) admits a unique solution on $[0, T]$. By Lemma 3.4, it suffices to show that $\mathbf{v}_t := F(t, \mu_t)$ satisfies (3.5) and (3.6). For the first, note that

$$\begin{aligned} \int_0^T \int_{\mathbb{R}^d} \|\mathbf{v}_t(x)\|_2 d\mu_t(x) dt &\leq \int_0^T \int_{\mathbb{R}^d} [\|\mathbf{v}_t(0)\|_2 + \|\mathbf{v}_t(x) - \mathbf{v}_t(0)\|_2] d\mu_t(x) dt \\ &\leq \int_0^T \int_{\mathbb{R}^d} [\|\mathbf{v}_t(0)\|_2 + L_1 \|x\|_2] d\mu_t(x) dt \\ &= \int_0^T \|\mathbf{v}_t(0)\|_2 dt + L_1 \int_0^T \int_{\mathbb{R}^d} \|x\|_2 d\mu_t(x) dt. \end{aligned}$$

We assume $(t, x) \mapsto \mathbf{v}_t(x)$ is C^1 , so

$$\int_0^T \|\mathbf{v}_t(0)\|_2 dt < \infty,$$

and $t \mapsto \int_{\mathbb{R}^d} \|x\|_2 d\mu_t(x)$ is continuous because $t \mapsto \mu_t$ is continuous with respect to W_2 , so

$$\int_0^T \int_{\mathbb{R}^d} \|x\|_2 d\mu_t(x) dt < \infty.$$

Hence, we have (3.5). For (3.6), if $B \subset \mathbb{R}^d$ is compact, then

$$\int_0^T \left(\sup_{x \in B} \|\mathbf{v}_t(x)\|_2 + \text{Lip}(\mathbf{v}_t, B) \right) dt \leq T \left(\sup_{t \in [0, T], x \in B} \|\mathbf{v}_t(x)\|_2 + L_1 \right) < \infty$$

again because $(t, x) \mapsto \mathbf{v}_t(x)$ is C^1 . By Lemma 3.4, the ODE (3.7) has a globally defined solution γ_x for μ_0 -a.e. $x \in \mathbb{R}^d$, and since $(x, t) \mapsto \mathbf{v}_t(x)$ is C^1 , γ_x is C^2 for such x .

Now, for

$$M := \left(\int_{\mathbb{R}^d} \max_{r \in [0, T]} \|\gamma_x''(r)\|_2^2 d\mu_0(x) \right)^{\frac{1}{2}} < \infty,$$

we will show

$$W_2(\mu_{(n+1)}, \mu_{t_{n+1}}) \leq (1 + H(L_1 + L_2))W_2(\mu_{(n)}, \mu_{t_n}) + \frac{H^2}{2}M. \quad (3.10)$$

By the triangle inequality for W_2 , we have

$$\begin{aligned} W_2(\mu_{(n+1)}, \mu_{t_{n+1}}) &= W_2((\text{id} + HF(t_n, \mu_{(n)}))\# \mu_{(n)}, \mu_{t_{n+1}}) \\ &\leq W_2((\text{id} + HF(t_n, \mu_{(n)}))\# \mu_{(n)}, (\text{id} + HF(t_n, \mu_{t_n}))\# \mu_{(n)}) \quad (*) \\ &\quad + W_2((\text{id} + HF(t_n, \mu_{t_n}))\# \mu_{(n)}, (\text{id} + HF(t_n, \mu_{t_n}))\# \mu_{t_n}) \quad (\dagger) \\ &\quad + W_2((\text{id} + HF(t_n, \mu_{t_n}))\# \mu_{t_n}, \mu_{t_{n+1}}). \quad (\ddagger) \end{aligned}$$

Handling each term separately, we have

$$\begin{aligned}
(*) &\leq \|(\text{id} + HF(t_n, \mu_{(n)})) - (\text{id} + HF(t_n, \mu_{t_n}))\|_{L^2(\mu_{(n)})} \\
&= H \|F(t_n, \mu_{(n)}) - F(t_n, \mu_{t_n})\|_{L^2(\mu_{(n)})} \\
&\leq HL_2 W_2(\mu_{(n)}, \mu_{t_n})
\end{aligned}$$

$$\begin{aligned}
(\dagger) &\leq \|\text{id} + HF(t_n, \mu_{t_n})\|_{\text{Lip}} W_2(\mu_{(n)}, \mu_{t_n}) \\
&\leq (1 + HL_1) W_2(\mu_{(n)}, \mu_{t_n})
\end{aligned}$$

$$(\ddagger) \leq \frac{H^2}{2} M,$$

where we used Theorem 3.9 for the last term.

Now, we recall the following elementary fact: If $\beta \geq 0$, $\alpha > 0$, and $(a_n)_{n \in \mathbb{N}}$ is a sequence of nonnegative numbers satisfying the recursive property that $a_{n+1} \leq (1 + \alpha)a_n + \beta$, then

$$a_n \leq e^{n\alpha} \left(a_0 + \frac{\beta}{\alpha} \right) - \frac{\beta}{\alpha}.$$

Applying this to (3.10) with $\alpha = H(L_1 + L_2)$ and $\beta = \frac{H^2}{2} M$ gives

$$W_2(\mu_{(n)}, \mu_{t_n}) \leq \frac{HM}{2(L_1 + L_2)} \left(e^{nH(L_1 + L_2)} - 1 \right),$$

as desired. □

3.3 Euler's Method with Imperfect Information

The above discussion shows that, under sufficient regularity assumptions, Euler's method on the Wasserstein manifold can approximate solutions to the continuity equation with tangent field prescribed by a "vector field" F . However, as discussed in Section 3.1, we rarely have access to F in practice, so we cannot explicitly compute the velocity field to be used in Euler's method. Instead, we will only have access to some oracle E_h that, given a time t and a measure μ , will return an approximation of what that measure would be at time $t + h$ if allowed to evolve according to F for some small time step h . That is, if μ is a solution to the continuity equation with $\mathbf{v}_t = F(t, \mu_t)$, then the oracle is such that

$$E_h(t, \mu_t) \approx \mu_{t+h}.$$

To perform an Euler-type method, then, we must first approximate the appropriate velocity field, and (2.11) hints that we should approximate it with

$$\mathbf{v}_t^h(x) := \frac{T_{\mu_t}^{E_h(t, \mu_t)}(x) - x}{h} \approx \frac{T_{\mu_t}^{\mu_{t+h}}(x) - x}{h}.$$

Unfortunately, even if $E_h(\mu_t) = \mu_{t+h}$ exactly, the L^2 convergence in (2.11) is not enough to guarantee that $\mathbf{v}_t^h(x) \rightarrow \mathbf{v}_t(x)$ pointwise as $h \rightarrow 0$. However, the L^2 convergence is still good enough to give a reasonable bound on the local truncation error of using this finite difference approximation in Euler's method.

Corollary 3.11. *Suppose $\mu_t \ll \mathcal{L}^d$ and $h > 0$. Set*

$$\mathbf{v}_t^h(x) := \frac{T_{\mu_t}^{E_h(t, \mu_t)}(x) - x}{h}.$$

Then

$$W_2(\mu_{t+H}, (\text{id} + H\mathbf{v}_t^h)_{\#}\mu_t) \leq H\|\mathbf{v}_t - \mathbf{v}_t^h\|_{L^2(\mu_t)} + o(H) \quad (3.12)$$

as $H \rightarrow 0$, and if $E_h(t, \mu_t) = \mu_{t+h}$, then $\|\mathbf{v}_t - \mathbf{v}_t^h\|_{L^2(\mu_t)} \rightarrow 0$ as $h \rightarrow 0$.

Proof. First note that (2.11) says that $\|\mathbf{v}_t - \mathbf{v}_t^h\|_{L^2(\mu_t)} \rightarrow 0$ as $h \rightarrow 0$ when $E_h(t, \mu_t) = \mu_{t+h}$.

For the inequality, by (2.10) we have

$$\begin{aligned} W_2(\mu_{t+H}, (\text{id} + H\mathbf{v}_t^h)_{\#}\mu_t) &\leq W_2(\mu_{t+H}, (\text{id} + H\mathbf{v}_t)_{\#}\mu_t) + W_2((\text{id} + H\mathbf{v}_t)_{\#}\mu_t, (\text{id} + H\mathbf{v}_t^h)_{\#}\mu_t) \\ &\leq o(H) + \|(\text{id} + H\mathbf{v}_t) - (\text{id} + H\mathbf{v}_t^h)\|_{L^2(\mu_t)} \\ &= o(H) + H\|\mathbf{v}_t - \mathbf{v}_t^h\|_{L^2(\mu_t)}. \quad \square \end{aligned}$$

This is the local truncation error of the Euler-type method

$$\mu_{(0)} = \mu_0, \quad \mu_{(n+1)} = (\text{id} + H\mathbf{v}_t^h)_{\#}\mu_{(n)}. \quad (3.13)$$

As was alluded to in Section 3.1, the local truncation error of this method depends on the accuracy of the approximation of the “tangent vector” $\mathbf{v}_t = F(t, \mu_t)$.

4 Euler-type Method for Empirical Measures of Particle Systems

The results in Section 3 show that an Euler-type scheme can effectively predict the evolution of a measure-valued curve (under certain conditions) even with incomplete knowledge of the underlying “dynamics” governing the curve’s evolution. In practical applications, one is often interested in predicting the evolution of (random) systems of particles $\{x_i(t)\}_{i=1}^N$ in \mathbb{R}^d . In such cases, the measure-valued curve one seeks to predict is the empirical measure

$$t \mapsto \mu_t^N := \frac{1}{N} \sum_{i=1}^N \delta_{x_i(t)},$$

and the oracle-type information one has is a particle-wise micro-scale simulation. Using this particle-wise simulation, we can construct an “oracle operator” E_h on discrete measures. If $\nu = \frac{1}{N} \sum_{i=1}^N \delta_{y_i}$ is a discrete measure, then $E_h(\nu) := \frac{1}{N} \sum_{i=1}^N \delta_{z_i}$, where $\{z_i\}_{i=1}^N$ is the output of running the micro-scale simulation for time h initialized with particles at the locations $\{y_i\}_{i=1}^N$. With this oracle in hand, we may hope to apply the Euler-type method described in Section 3.3 to μ^N . Specifically, if

$$\mathbf{v}_t^{h,N}(x_i(t)) := \frac{T_{\mu_t^N}^{E_h(\mu_t^N)}(x_i(t)) - x_i(t)}{h} \quad i = 1, \dots, N, \quad (4.1)$$

$$\tilde{\mu}_{t+H}^N := \left(\text{id} + H\mathbf{v}_t^{h,N} \right)_{\#} \mu_t^N = \frac{1}{N} \sum_{i=1}^N \delta_{x_i(t) + H\mathbf{v}_t^{h,N}(x_i(t))}, \quad (4.2)$$

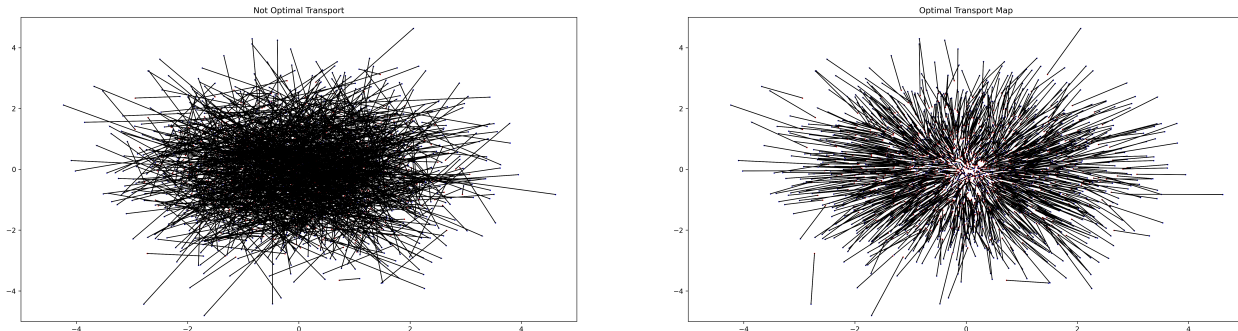


Figure 4.1: Example of the difference between the optimal transport map and the particle-wise map. In the particle-wise image (left), an arrow is drawn to connect each particle’s starting position to its ending position. In the optimal transport image (right), we compute the OT map between the starting and ending distributions and draw an arrow connecting each particle’s starting location to its corresponding output under the OT map.

then we may hope that $\tilde{\mu}_{t+H}^N \approx \mu_{t+H}^N$. Unfortunately, none of the theory from Section 3 applies in this setting: μ_t^N clearly does not have a density, and in many systems of interest, the particles’ evolution is too rough in time for the curve μ^N to be absolutely continuous. (Suppose x_i is, e.g., a Brownian motion.) In particular, μ^N has no tangent field, so there is no reason to believe that $\mathbf{v}^{h,N}$ can tell us anything about the true value μ_{t+H}^N . The key idea of our examples is to sidestep this major issue by assuming that μ^N is an empirical estimate of a “nice” curve μ with velocity field \mathbf{v} . In this case, $\mu^N \approx \mu$ for large N , and the hope is that $\mathbf{v}^{h,N} \approx \mathbf{v}$ in such a way that ensures $\tilde{\mu}_{t+H}^N \approx \mu_{t+H}^N$. While work on proving precise results of this form is ongoing, we give empirical evidence that the approach works in Sections 5 and 6. At a heuristic level, even though no tangent field describes the evolution of μ_t^N on short time scales, there is still a notion of a “direction” — determined by μ — in which the *group* of particles is traveling over longer time scales. The idea is that optimal transport maps allow us to access that direction.

As an illustrative example, suppose the x_i are independent, standard d -dimensional Brownian motions, the smooth curve “in the background” is $t \mapsto \mu_t := \mathcal{N}(0, tI_d)$, and the oracle is given by an Euler–Maruyama simulation of Gaussian diffusion:

$$E_h(\nu) = \frac{1}{N} \sum_{i=1}^N \delta_{y_i + \sqrt{h}Z_i}, \quad (4.3)$$

where $\nu = \frac{1}{N} \sum_{i=1}^N \delta_{y_i}$ and $Z_1, \dots, Z_N \sim \mathcal{N}(0, I_d)$ are i.i.d. By Theorem 2.6(iii), the tangent field \mathbf{v} of μ is given by

$$\mathbf{v}_t(x) = \lim_{h \rightarrow 0} \frac{T^{\mu_{t+h}}(x) - x}{h} = \lim_{h \rightarrow 0} \frac{\sqrt{\frac{t+h}{t}} - 1}{h} x = \frac{x}{2t}. \quad (4.4)$$

Now, see Figure 4.1, in which $d = 2$. In the first image, an arrow is drawn from $x_i(1)$ to $x_i(1) + Z_i$, and the arrows are expectedly chaotic. In contrast, the arrows in the second image are drawn from $x_i(1)$ to $x_i(1) + \mathbf{v}_1^{1,N}(x_i(1))$ in accordance with our measure-valued Euler-type method, which reveals the obvious structure of the evolution: The bulk is drifting away from the center in all directions, which agrees with what (4.4) suggests.

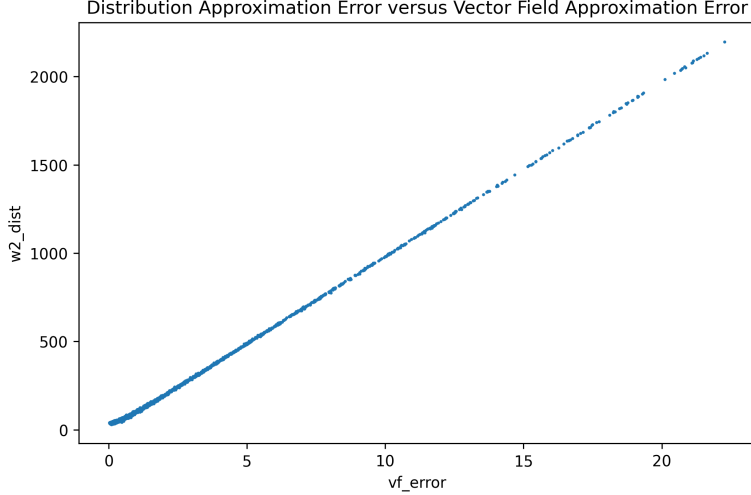


Figure 4.2: Vector field approximation error $\|\mathbf{v}_t - \mathbf{v}_t^{h,N}\|_{L^2(\mu_t^N)}^2$ versus Euler step approximation error $W_2(\mu_{t+H}^N, \tilde{\mu}_{t+H}^N)^2$ for Brownian motion with $t = 1$ and $H = 99$ (h and N vary)

4.1 Choosing an Appropriate Step Size

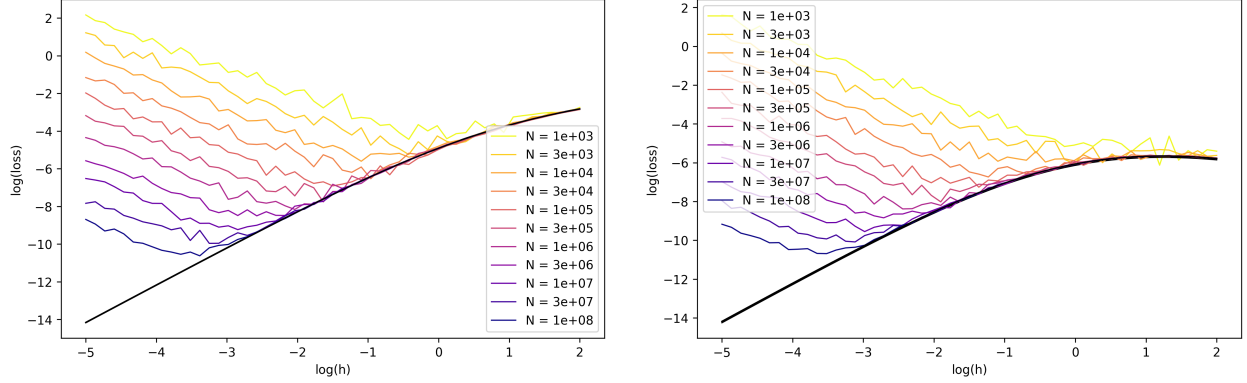
In the “smooth” case, the error of the approximation $\mu_{t+H} \approx (\text{id} + H\mathbf{v}_t^h)_\# \mu_t$ generically decreases as h decreases. In the discrete case, however, the roughness of our particles’ evolutions introduces a competing need to keep h sufficiently large. To explain why, recall from Proposition 2.4 that optimal transport maps in the discrete case are given by permutations. Assuming (as we always will) that the particles $\{x_i\}_{i=1}^N$ evolve continuously in time, if h is small enough, then the relevant permutation becomes the identity. More specifically, if h is very small, then running our micro-scale simulation for time h initialized at $x_i(t)$ will result in a particle $y_i^h \approx x_i(t+h)$ that is very close to $x_i(t)$. In this case, the map $x_i(t) \mapsto y_i^h$ will optimally transport μ_t^N to $E_h(\mu_t^N)$. Therefore,

$$\begin{aligned} \mathbf{v}_t^{h,N}(x_i(t)) &= \frac{T_{\mu_t^N}^{E_h(\mu_t^N)}(x_i(t)) - x_i(t)}{h} = \frac{y_i^h - x_i(t)}{h} \approx \frac{x_i(t+h) - x_i(t)}{h}, \\ \tilde{\mu}_{t+H}^N &= \frac{1}{N} \sum_{i=1}^N \delta_{x_i(t)+H\mathbf{v}_t^{h,N}(x_i(t))} \approx \frac{1}{N} \sum_{i=1}^N \delta_{x_i(t)+H\frac{x_i(t+h)-x_i(t)}{h}}. \end{aligned}$$

Since x_i is not necessarily differentiable at t , $x_i(t) + H\frac{x_i(t+h)-x_i(t)}{h}$ is not necessarily a good approximation of $x_i(t+H)$, so $\tilde{\mu}_{t+H}^N$ is not necessarily a good approximation of μ_{t+H}^N if h is too small.

To empirically verify the intuition that small choices of h result in poor approximations, we return to the case of Brownian motion. Specifically, suppose again that the x_i are independent Brownian motions in \mathbb{R}^d , $\mu_t = \mathcal{N}(0, tI_d)$, $\mathbf{v}_t(x) = \frac{x}{2t}$, and the oracle is given in terms of an Euler–Maruyama simulation. We have observed experimentally that the approximation error $W_2(\mu_{t+H}^N, \tilde{\mu}_{t+H}^N)^2$ is strongly correlated with the error $\|\mathbf{v}_t - \mathbf{v}_t^{h,N}\|_{L^2(\mu_t^N)}^2$ in the approximation of the underlying tangent field (Figure 4.2), so we focus the remaining discussion on the latter quantity for computational convenience.

There are two distinct sources of error in the tangent field approximation. The first is the error in



(a) True approximation error: The black curve is the log of theoretical finite difference error $\|\mathbf{v}_t - \mathbf{v}_t^h\|^2$ versus the log of the step size h . The colored curves are the log of the discrete approximation error $\|\mathbf{v}_t - \mathbf{v}_t^{h,N}\|^2$ for various values of N .

(b) Estimated approximation error: The black curve is the log of theoretical finite difference error $\|\mathbf{v}_t^h - \mathbf{v}_t^{2h}\|^2$ versus the log of the step size h . The colored curves are the log of the discrete approximation error $\|\mathbf{v}_t^{h,N} - \mathbf{v}_t^{2h,N}\|^2$ for various values of N .

Figure 4.3: Results of vector field error computations for Brownian motion and comparison with an estimated error using the difference between consecutive approximations

the approximation of a derivative by a finite difference with step $h > 0$; the second is the error in using a discrete optimal transport map to approximate a continuous one. As suggested above, the first should dominate for large values of h , and the second should dominate for small values of h . To isolate their effects, we also consider the finite-difference approximation of the tangent field \mathbf{v} ,

$$\mathbf{v}_t^h(x) = \frac{T_{\mu_t}^{\mu_{t+h}}(x) - x}{h} = \frac{\sqrt{\frac{t+h}{t}} - 1}{h}x,$$

and compute $\|\mathbf{v}_t - \mathbf{v}_t^h\|_{L^2(\mu_t^N)}$ as a proxy for the error caused by the finite-difference approximation. In Figure 4.3a, we plot $\|\mathbf{v}_1 - \mathbf{v}_1^h\|_{L^2(\mu_1^N)}$ in black and $\|\mathbf{v}_1 - \mathbf{v}_1^{h,N}\|_{L^2(\mu_1^N)}$ for different values of h, N in various other colors. We note that for each value of N , there is an approximately optimal value of h that minimizes the error and that this optimal value of h decreases as N increases. We also see that for very small values of h , the error is very large (as predicted above) and that for larger values of h , the discrete approximation is about as good as the true finite difference approximation. This indicates that, indeed, as the step size increases, the optimal transport map better captures the distribution's bulk behavior, and the limiting factor on choosing h too big is the fact that we are approximating a derivative using a finite difference. While these experiments do not precisely formalize this behavior, they corroborate the assertion that there should be a “happy-medium” value of h that decreases as the number of samples increases.

We expect this phenomenon to appear in most random particle systems one would be interested in studying using optimal transport. As such, one might hope to empirically determine the optimal choice for h to use in the prediction algorithm. Unfortunately, the previous paragraph's analysis was only possible because we had explicit a priori knowledge of \mathbf{v} , which defeats the purpose of approximating it. A different approach is therefore needed to determine the optimal step size h . To this end, we perform another experiment to assess the viability of a simple intrinsic criterion: how much the approximation of the vector field changes after another step of size h , i.e., $\|\mathbf{v}_1^{h,N} - \mathbf{v}_1^{2h,N}\|_{L^2(\mu_1^N)}$. In Figure 4.3b, we compare $\|\mathbf{v}_1^{h,N} - \mathbf{v}_1^{2h,N}\|_{L^2(\mu_1^N)}$ with $\|\mathbf{v}_1^h - \mathbf{v}_1^{2h}\|_{L^2(\mu_1^N)}$, the “normal”

difference between two consecutive finite-difference approximations. While the correspondence is not perfect, the plots are remarkably similar, which suggests the method’s potential use. Though we do not use this approach in our experiments in Sections 5 and 6 — we instead simply fix h as a parameter — one could imagine adaptations to the algorithm in Section 4.3 that dynamically adjust h using this heuristic.

Remark 4.5. *On a practical note, if the step size of the micro-scale simulator is fixed, then one can effectively increase h by taking E_h to be the result of applying multiple micro-scale steps in succession. This means we always have the flexibility to increase the effective value of h . Thus, it still makes sense to discuss how to tune h appropriately, even if the micro-scale simulator itself has a fixed time step.*

4.2 Additional Considerations

Statistical Averaging: When working with random particle systems, it is often advantageous to replace the single finite difference \mathbf{v}_t^h with an average of many finite differences. There are many ways to do this, but perhaps the simplest is to average finite differences computed with a range of different time steps over some interval. Also, if we take the middle of this interval to be the time of interest, then taking an average of both forward and backward differences becomes equivalent to taking an average of centered differences, which are typically more accurate numerically. Explicitly, for a fixed time step h and discrete times $t_0 - kh =: t_{-k}, \dots, t_0, \dots, t_k := t_0 + kh$, we set

$$\begin{aligned} \mathbf{v}_{t_0}^{h,N,k}(x_i(t_0)) &:= \frac{1}{2k} \sum_{\substack{j=-k \\ j \neq 0}}^k \mathbf{v}_t^{jh}(x_i(t_0)) \\ &= \frac{1}{2k} \sum_{\substack{j=-k \\ j \neq 0}}^k \frac{T_{\mu_{t_0}^N}^{\mu_{t_0}^N} (x_i(t_0)) - x_i(t_0)}{jh} \\ &= \frac{1}{k} \sum_{j=1}^k \frac{T_{\mu_{t_0}^N}^{\mu_{t_0}^N} (x_i(t_0)) - T_{\mu_{t_0}^N}^{\mu_{t_0}^N - j} (x_i(t_0))}{2jh}. \end{aligned}$$

This vector field is the one we use in practice in the experiments in Sections 5 and 6.

Burn-in Period: To approximate the particle distribution μ_t^N over a long time, we need to perform many steps of our Euler-type method. Of course, this involves re-initializing the micro-scale simulation many times, once after each step. One potential obstacle of this approach is that the approximate distribution after an Euler step will inevitably be slightly different from the true distribution, and running the micro-scale simulation on the approximate distribution might result in behavior that is initially dominated by the approximate distribution’s return to a relative equilibrium. To account for this and ensure the approximated velocity fields capture mostly the long-term dynamics, we allow the approximate distribution to evolve according to the micro-scale simulation for a prescribed “burn-in” time H_R before starting to take samples to approximate the velocity field at time $t + H + H_R$. This ensures that any fringe effects from the Euler step are washed away before the next Euler step. The burn-in period also helps to avoid the pathologies

that can arise from using Euler’s method on, e.g., Wasserstein gradient flows [31]. For example, there may be locations with a high density of approximated particles (or even particles with exactly the same approximated location), which can result in irregularities in the subsequent vector field approximation. By allowing the particle system to “burn in” after each approximating step, we ensure that the particles’ density is, loosely speaking, smoothed out. For an illustration of how the burn-in time allows the density to smooth, see Figures 5.2 and 5.3. Empirical tests indicate that this burn-in is essential for our method to work well. Understanding these benefits theoretically is a subject of ongoing work.

4.3 Detailed Description of Our Algorithm

Parameter	Description
h	the time of one step of the micro-scale simulation
k	the number of centered differences to average
$H_S := kh$	<i>half</i> the length of the derivative-sample time window
N_T	the number of Euler-type prediction steps
H	the length of each Euler step
H_R	the burn-in time after each Euler step
$\Delta := H_S + H + H_R$	the time difference between Euler steps
S	the length of start-up time
R	the length of final recovery time after all Euler steps

Table 4.1: Parameter definitions

Here is a description of the complete algorithm for approximating the distribution μ_T^N for large T with all the additional considerations discussed in this section. We fix values for the parameters as defined in Table 4.1 and then:

1. Run the micro-scale simulation for the start-up time S (by taking S/h micro-scale steps) to allow the initial distribution μ_0 to reach a relative equilibrium (if necessary). Call the initial distribution $\mu_{(-1)+H_R}$.
2. For each approximating step $n = 0, \dots, N_T$:
 - (a) Set $\mu_{(n)-kh} := \mu_{(n-1)+H_R}$, and take $2k$ micro-scale steps to get distributions

$$\mu_{(n)-kh}^N, \dots, \mu_{(n)}^N, \dots, \mu_{(n)+kh}^N.$$

- (b) For each x_i in the support of $\mu_{(n)}^N$, compute

$$\mathbf{v}_{(n)}^{h,N,k}(x_i) := \frac{1}{k} \sum_{j=1}^k \frac{T^{\mu_{(n)}^N + jh}(x_i) - T^{\mu_{(n)}^N - jh}(x_i)}{2jh}$$

(c) Set

$$\mu_{(n)+H}^N := \left(\text{id} + \mathbf{v}_{(n)}^{h,N,k} \right)_{\#} \mu_{(n)}^N.$$

(d) Take H_R/h micro-scale steps to allow the distribution to burn in. Call the resulting distribution $\mu_{(n)+H_R}^N$.

3. Run the micro-scale simulation for some final recover time R (by taking R/h micro-scale steps) to ensure any fringe errors in the approximations are minimized (e.g., that the distribution has indeed reached a true steady state).

While the notation used above is convenient for highlighting the recursive nature of the algorithm, it becomes unwieldy when discussing how to interpret the approximations. As such, we set the following notation convention:

Notation 4.6. Let $\tilde{\mu}_t^N$ denote the approximation produced by the algorithm that corresponds to time t .

More explicitly, if $t_n := S + n(H_S + H + H_R) + H_S$, then $\tilde{\mu}_{t_n}^N = \mu_{(n)}^N$ is the approximation we use to compute the Euler step, $\tilde{\mu}_{t_n+H}^N = \mu_{(n)+H}^N$ is the approximation immediately after the Euler step, and $\tilde{\mu}_{t_n+H+H_R}^N = \mu_{(n)+H_R}^N$ is the approximation after the burn-in period. This notation is convenient because $\tilde{\mu}_t^N$ is an approximation of μ_t^N for all t for which the former is defined.

Remark 4.7. The above scheme reduces the number of micro-scale steps required to reach the desired end time (as compared to equivalent simulations that only use micro-scale steps) by a factor of $\frac{2H_S+H_R}{H_S+H_R+H}$, so ideally we would like to have $H \gg 2H_S + H_R$ so that the speed-up is nontrivial. Experiments on some illustrative examples (Sections 5 and 6) demonstrate that with well-chosen values, the above scheme works well to predict long-term behavior while also giving meaningful speed-up.

Remark 4.8. One limitation of this scheme that will become relevant in Section 6 is that it only gives a way to approximate future locations of particles and not any underlying data. If the micro-scale model has any parameters besides the position of the particles (e.g., the current “underlying state” of a particle), then these data must also be predicted across the Euler-type predicting step taken in step 2(c) above. In general, there is no single method for doing this, but we will discuss ad hoc approaches as they come up in Section 6 where we must also predict the state of the bacteria’s flagella and other underlying data (see Sections 6.2 and 6.4).

5 Experiments with Reflected Brownian Motion

As a proof of concept demonstrating its efficacy, we use our algorithm to simulate reflected Brownian motion (RBM) in a rectangle $[x_{\min}, x_{\max}] \times [x_{\min}, x_{\max}]$, which approaches a steady state that is uniform on $[x_{\min}, x_{\max}] \times [x_{\min}, x_{\max}]$ as time approaches infinity. The oracle is defined similarly to (4.3) except that if any point in the support of $E_h(\nu)$ is outside the allowed rectangle, then we reflect it across the nearest boundary (and repeat if necessary). We also take $Z_i \sim \mathcal{N}(0, \frac{1}{64}I_d)$ instead of $Z_i \sim \mathcal{N}(0, I_d)$ to round out some of the numbers, which means we are actually simulating RBM with time slowed down by a factor of 1/64. We reiterate from the introduction that this system’s oracle (i.e., the Euler–Maruyama simulation of RBM) is already computationally cheap over long time

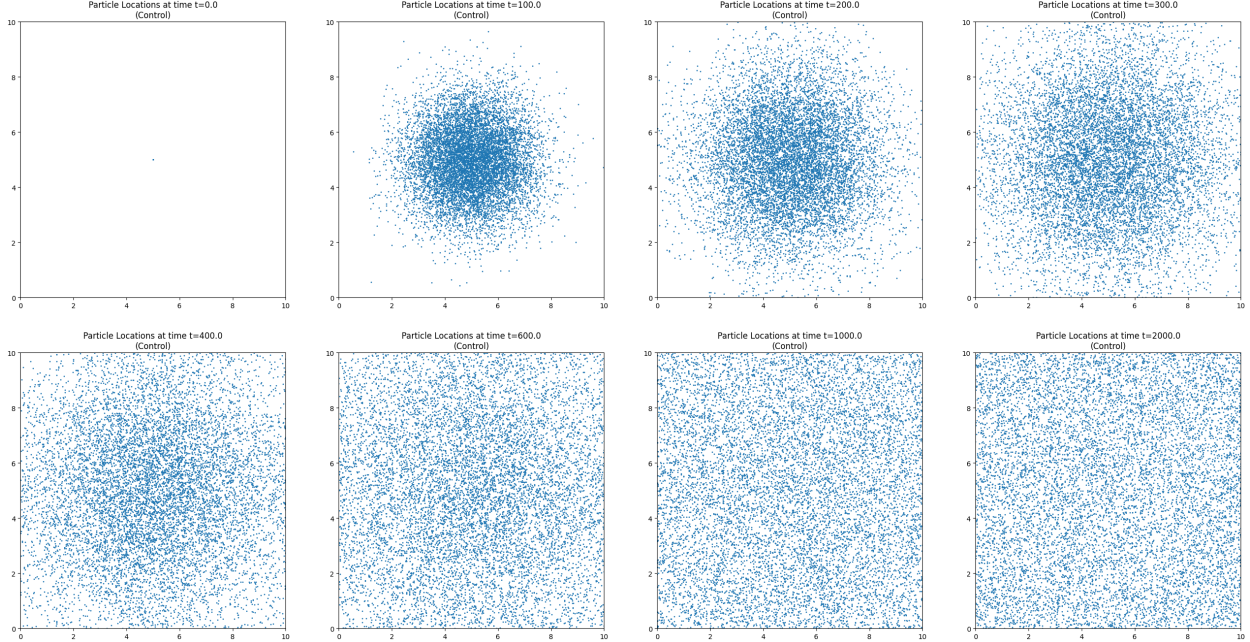


Figure 5.1: Scatter plots of particle locations at various times t from $t = 0$ to $t = 2000$ for the control simulation of 2-D RBM

scales, so in practice, there is no computational benefit to using our algorithm in this case. A more computationally expensive micro-scale simulation where our algorithm *does* provide computational speed-ups is given in Section 6.

Before running the approximation algorithm, we run the aforementioned Euler–Maruyama micro-scale simulation from $t = 0$ to $t = T$ with the parameters shown in Table 5.1. (The end time is chosen long enough to effectively reach steady state.) Figure 5.1 shows scatter plots of the particles over time. We consider these data the “controls” and compare the results of our approximation algorithm to these control distributions.

We then run the approximation algorithm with the same parameters as in Table 5.1 and the additional parameters (defined in Section 4.3) in Table 5.2. Note that the effective end time of this simulation is $T = S + N_T(H_S + H + H_R) + R = 2000$, which agrees with the control simulations.

Parameter	Description
$N = 10,000$	number of independent particles
$h = 1/16$	micro-scale simulation step size
$x_i(0) = (5, 5) \quad \forall i = 1, \dots, N$	initial particle locations
$[x_{\min}, x_{\max}] \times [x_{\min}, x_{\max}] = [0, 10] \times [0, 10]$	domain bounds
$T = 2000$	end time

Table 5.1: Parameters for 2-D RBM micro-scale simulation

Parameter	Description
$S = 30$	length of start-up time
$k = 80$	number of centered differences to average
$H = 85$	length of each Euler-type prediction step
$H_R = 30$	burn-in time after each Euler step
$N_T = 16$	number of Euler steps
$R = 50$	length of final recovery time after last Euler step

Table 5.2: Additional parameters for approximation algorithm with 2-D RBM

Figure 5.2 shows the distributions obtained after the first two Euler steps ($t = 120, 240$), the distributions after the $H_R = 30$ burn-in time ($t = 150, 270$), and the distributions from the control simulation at the corresponding times for comparison. Similarly, Figure 5.3 shows the last two Euler steps ($t = 1800, 1920$) and corresponding burn-in times ($t = 1830, 2000$ — recall that the last burn-in time has an additional final recovery of $R = 50$). In both figures, we note that the distributions immediately after the Euler steps look very different from the control distributions at the corresponding time; the density of points is not as smooth as it should be. As mentioned in Section 4.2, this is exactly the point of the burn-in time.

Looking at Figure 5.2, we can see that the burn-in time of $H_R = 30$ seems to be long enough for the distribution to qualitatively return to a smooth Gaussian. This corresponds to the distribution’s having reached a relative equilibrium, at which point the long-term dynamics once again dominate the behavior of the distribution. Accurately determining when this occurs is critical to selecting an optimal value for the duration of the burn-in window. Our current approach is to pick this value based on previously observed experimental data, but one could devise other algorithms that adaptively determine the recovery time.

Remark 5.1. *The burn-in time needs to be relatively lengthy here because the particles tend to “clump together” after each Euler step. We believe this behavior is caused by the approximated vector field $\mathbf{v}_t^{k,N,h}$ not being “smooth enough,” as other experimental evidence suggests that smoother vector fields yield smoother Euler approximations. Thus, this clumping could likely be reduced by, e.g., first applying a kernel smoothing technique to $\mathbf{v}_t^{k,N,h}$, and doing so could drastically reduce the burn-in time required for the distribution to return to a relative equilibrium. Further work experimenting in this direction is ongoing.*

To assess the accuracy of the approximations, we compute the Wasserstein distance between the control distribution μ_t^N and the approximated distribution $\tilde{\mu}_t^N$. A plot of the distance $W_2(\mu_t^N, \tilde{\mu}_t^N)$ versus time t (for the discrete set of times from our experiments) is shown in Figure 5.4a. We also visualize how well the approximations track the true curve $t \mapsto \mu_t^N$ by embedding into a common linear space and performing a dimension reduction. Specifically, we (1) fix a common (discrete) reference measure σ (in our case, by choosing $N = 10,000$ independent samples of a standard Gaussian); (2) compute optimal transport maps $T_\sigma^{\mu_t^N}$ and $T_\sigma^{\tilde{\mu}_t^N}$; (3) vectorize $T_\sigma^{\mu_t^N}$ and $T_\sigma^{\tilde{\mu}_t^N}$ by interpreting them as $N \times d$ matrices, where N is the number of particles in σ and d is the ambient dimension (two in our case); and (4) perform PCA to project onto a two-dimensional subspace. The results are shown in Figure 5.4b.

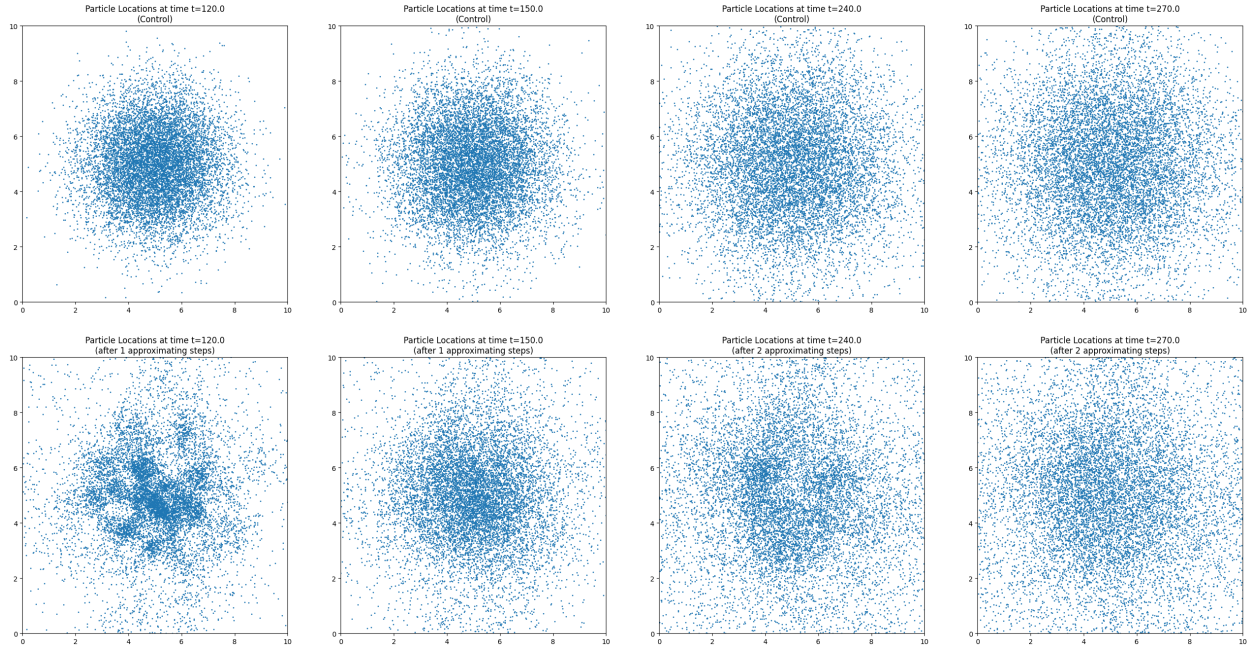


Figure 5.2: Scatter plots of particle locations after first two Euler steps (bottom) compared with corresponding times from control simulation (top). We run the micro-scale simulation until $t = 30$ (not pictured), take an Euler step to $t = 120$ (leftmost), burn in until $t = 150$ (second from left), take an Euler step to $t = 240$ (second from right), and burn in until $t = 270$ (rightmost).

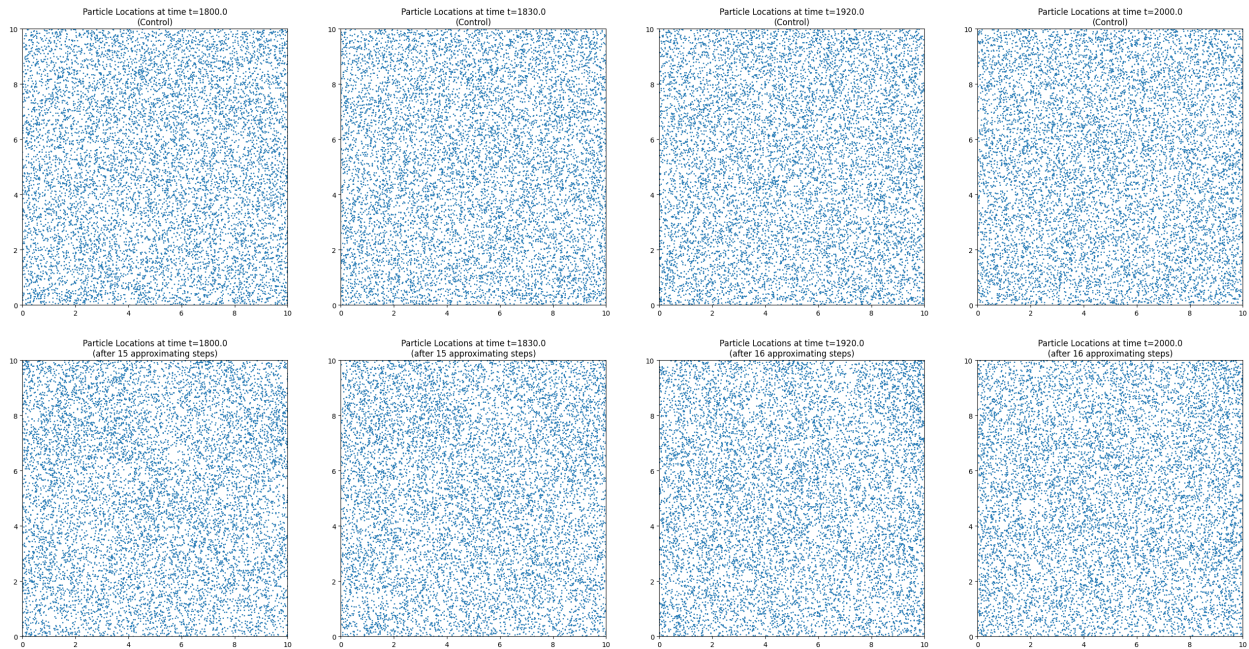
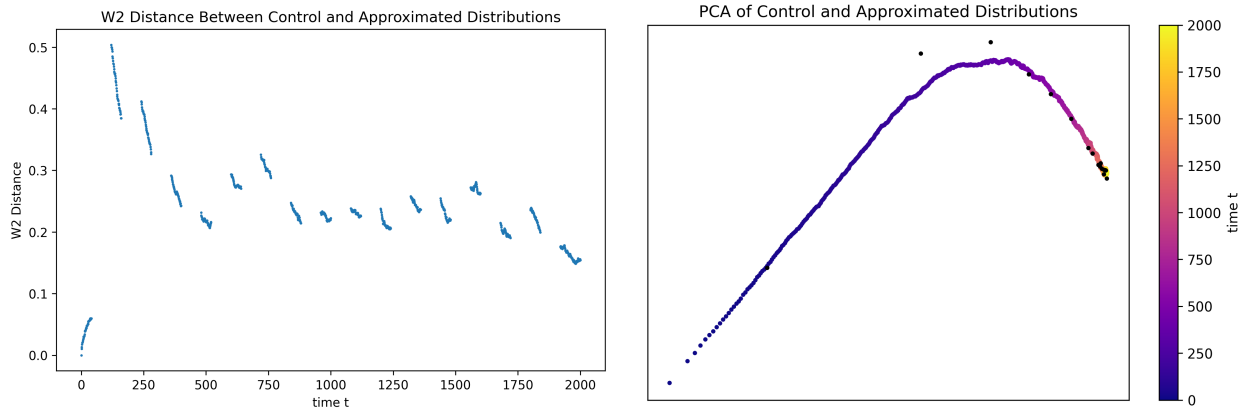


Figure 5.3: Scatter plots of particle locations after final two Euler steps (bottom) compared with corresponding times from control simulation (top). We take an Euler step from $t = 1710$ (not pictured) to $t = 1800$ (leftmost), burn in until $t = 1830$ (second from left), take an Euler step to $t = 1920$ (second from right), and finally recover until $t = 2000$ (rightmost), the end time.



(a) 2-Wasserstein distance between control distribution and approximated distributions versus time

(b) Projections of distributions onto the two principal components of the control distribution's evolution over time. The solid rainbow curve shows the control distribution, where the color represents time according to the color bar at the right. The black dots represent the approximations after the burn-in period.

Figure 5.4: Comparisons between control distributions and approximations

Finally, to exhibit the benefit of using optimal transport, we compare the above experiments to equivalent particle-wise experiments. Specifically, we can perform the finite-difference calculations on the individual particles in the system:

$$x_i^{[1],h,k}(t) := \frac{1}{k} \sum_{j=1}^k \frac{x_i(t+jh) - x_i(t-jh)}{2jh}, \quad i = 1, \dots, N.$$

Effectively, this attempts to approximate $x_i'(t)$ (ignoring that this derivative does not exist). Then we can use these finite differences to form the Euler-type approximation

$$\tilde{x}_i(t+H) := x_i(t) + Hx_i^{[1],h,k}(t), \quad i = 1, \dots, N.$$

As explained in Section 4.1, this approach should result in a much worse approximation of the overall distribution's evolution. Our experiments agree with this prediction. Figure 5.5 shows the result of the first two Euler steps using the particle-wise approach (with the same parameters). The approximated distribution immediately becomes uniform and does not match the corresponding control distribution at all. This demonstrates that the optimal transport maps are an essential component of our algorithm's success.

6 Experiments with Bacterial Chemotaxis

The experiments in Section 5 indicate that if the particles approximate a continuous distribution that evolves according to a smooth vector field, then the discrete vector field approximates the underlying smooth one, and our algorithm can correctly predict the long-term collective evolution of the particles. This leads us to believe that even if the underlying distribution is unknown, as long as it evolves according to *some* underlying vector field, then our algorithm will still reasonably

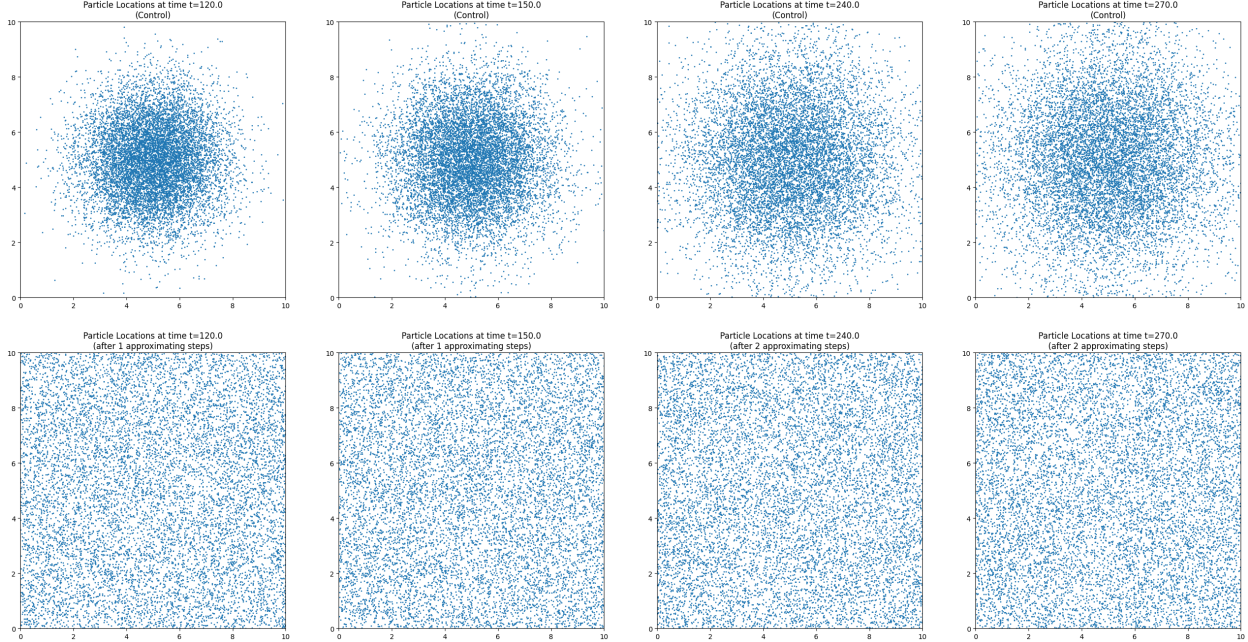


Figure 5.5: Scatter plots of particle locations after the first two particle-wise Euler steps (bottom) compared with corresponding times from the control simulation (top)

approximate the long-term behavior of the system. To this end, we now present an example of performing our algorithm on a micro-scale simulation for which we actually do not know the underlying vector field. As we will see, it is a reasonable assumption based on experimental data that the underlying dynamics behave nicely and that the evolution of the “true” distribution is smooth, but we cannot explicitly verify this fact theoretically. Additionally, the micro-scale simulation is computationally expensive, so our algorithm does actually speed up the computation time required to simulate the long-term behavior. Thus, this experiment will demonstrate that our algorithm can indeed be successful without a priori assumptions on the system dynamics, and it can also speed up simulations without severely sacrificing accuracy.

6.1 Problem Setup

The experiments described in Section 5 have the simple property that the micro-scale simulation only depends on the locations of the particles. This time independence allows us to approximate large-time steps within reasonable error bounds. However, some micro-scale models, such as bacterial locomotion by chemoattractant, are intertwined with other spatiotemporal variables, like a chemoattractant profile. As a result, a proper re-initialization of the micro-scale properties at the predicted location is required for an approximation of a large time step of all dependent variables, leading to a challenging problem.

In order to demonstrate the efficacy of the suggested approximation algorithm in a complex micro-scale simulation, we have applied the method to a biological application — the chemotactic movement of bacteria. The mobility of bacteria is affected by the presence of chemoattractant (specifically, its spatial derivative). However, when we approximate the location of bacteria after a large

Parameter	Description
$N = 10,000$	the number of bacteria (the number of simulations)
$x \in \mathbb{R}^d$	d -dimensional position vector for each bacteria
$s^{(i)} \in \{0, 1\}, (i = 1, \dots, 6)$	indicator of rotating direction of flagella ($s^{(i)} = 0$ clockwise or $s^{(i)} = 1$ counterclockwise. If more than three flagella are rotating counterclockwise, bacteria start moving.)
$h = 1/16$	microscopic time step
$v_{\text{cell}} = 0.003$	the swimming speed of each bacteria
$S(x) = \text{NormPDF}(\mu = 6.5, \sigma = 1.35)$	chemoattractant profile

Table 6.1: Parameters for chemotaxis micro-scale simulation

Parameter	Description
$S = 200$	length of start-up time
$k = 80$	number of centered differences to average
$H = 95$	length of each Euler-type prediction step
$H_R = 100$	burn-in time after each Euler step
$N_T = 19$	number of Euler steps
$R = 0$	length of final recovery time after last Euler step

Table 6.2: Additional parameters for approximation algorithm with chemotaxis micro-scale simulation

time step, we may lose the actual trajectory of the bacteria due to a lack of information about the chemotactic effect, resulting in inaccurate predictions. If the chemoattractant profile is smooth enough in space, the microscopic properties of bacteria can be re-initialized within a short recovery time and then follow slow dynamics.

The chemotactic mobility of bacteria has been simulated using a microscopic and stochastic simulator [27, 18]. In this paper, we provide only a brief description of variables and a summary of the setup for this micro-simulator in Table 6.1. For more theoretical and technical details, please refer to the cited papers.

6.2 Experimental Results

For reference, we run the simulation without prediction to establish a “control” as the ground truth behavior of the system. We use the same parameters as in [27, 18] with only the changes specified in Table 6.1. Histograms of bacteria positions at different times in the control simulation are shown in Figure 6.1. Then, to compare with the control data, we perform a simulation using the approximation algorithm with the additional parameters in Table 6.2.

To continue simulating after each Euler step, the micro-scale simulator requires not only current bacteria locations but also all microscopic quantities. However, as discussed in Remark 4.8, the

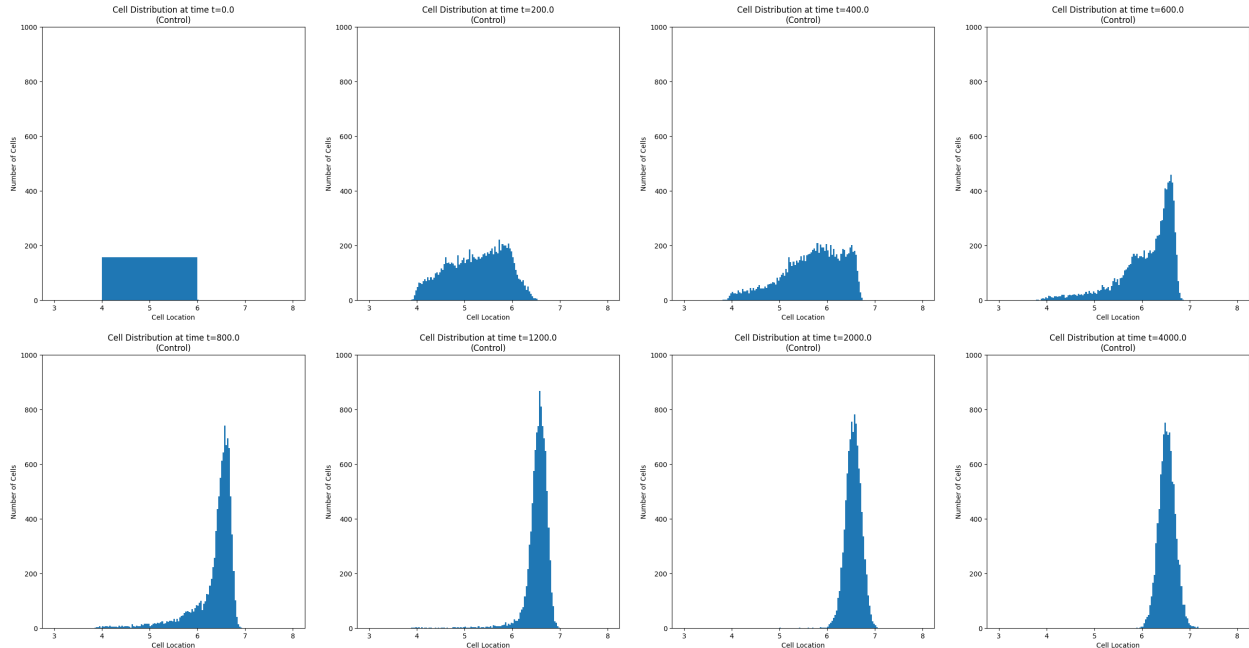


Figure 6.1: Histograms of bacteria locations, with a bin width of 0.04, at various times t from $t = 0$ to $t = 4000$ for the control simulation of chemotaxis

algorithm described in Section 4.3 predicts only the *locations* of bacteria after each Euler step, resulting in a lack (or missing) of microscopic quantities. Hence, after the predicting time step, the suggested algorithm requires the re-initialization of microscopic quantities, such as u_1, u_2 , and $s^{(i)}$. Even though some (quantitatively bad but) qualitatively good re-initializations quickly reach slow dynamics, we suggest a better re-initialization scheme based on the history of microscopic quantities and demonstrate a more accurate prediction of bacteria density distribution over multiple Euler steps.

After each Euler step, we re-initialize the underlying data according to the history-dependent scheme in Table 6.3. For example, given data at time t_0 , we use the optimal transport approximation scheme to predict the bacteria locations at $t_0 + H$ and re-initialize the microscopic properties at $t_0 + H$ as follows:

- Set $u_1 = 0$ for all bacteria,
- compute $u'_2(t_0) = \frac{du_2}{dt} \Big|_{t=t_0}$ from the prescribed ODE in [27] to take a forward Euler step $\tilde{u}_2(t_0 + H) := u_2(t_0) + H \cdot u'_2(t_0)$, and
- keep the flagella rotating direction and bacteria moving direction exactly the same as they were at time t_0 .

Figures 6.2 and 6.3 show qualitative histograms of the control and approximation distributions of the bacteria locations after the first two and last two Euler steps.

Parameters	History-Dependent Scheme	History-Independent Scheme
u_1	$\tilde{u}_1(t_0 + H) := 0$	$\tilde{u}_1(t_0 + H) := 0$
u_2	$\tilde{u}_2(t_0 + H) := u_2(t_0) + H \cdot u_2'(t_0)$	$\tilde{u}_2(t_0 + H) := f(S(\tilde{x}(t_0 + H)))$
$s^{(i)}$	$\tilde{s}^{(i)}(t_0 + H) := s^{(i)}(t_0)$	$\tilde{s}^{(i)}(t_0 + H) := 0$ (fixed)

Table 6.3: Parameters of different re-initialization schemes. The “history-dependent” scheme (as suggested in this paper) retains the flagella states from the micro-scale simulation immediately before the Euler step, and it attempts to predict u_2 via an Euler forward step. The “history-independent” scheme (described in [27]) sets a fixed number of flagella to rotate counterclockwise (here, 0), and u_2 is set solely as a function of the predicted location of bacteria.

6.3 Computational Improvement

Compared with the control simulation, our algorithm requires 11/20 as many micro-scale steps (10 seconds of velocity-field-approximation and 100 seconds of burn-in time for every 200 seconds of simulated time). Despite the relatively long burn-in time, this still decreases the overall computation time by roughly half because the cost of computing the optimal transport maps (which in 1-D simply requires sorting the bacteria locations) is small compared with the cost of performing the micro-scale steps. Thus, the overall computation time required to perform the approximation algorithm is roughly 11/20 of the time required to perform the control simulation. This is indeed what we see experimentally: On one machine, the control simulation takes about 30 minutes to run, and the approximation algorithm takes about 17 minutes.

The primary way this speed-up could be improved is by decreasing the burn-in time or increasing the length of the Euler step. We have experimentally observed that with our choice of re-initialization, the burn-in time required for the underlying variables to return to relative equilibrium scales roughly with the size of the Euler step. This means that achieving better speed improvements likely requires a better approach to re-initializing the underlying variables. We have seen in further experiments (omitted for brevity) that the burn-in time can be reduced considerably if the underlying variables are re-initialized perfectly, e.g., by using data from the control simulation. This suggests that the current barrier to more significant speed improvements is the quality of re-initializations, not the quality of the distribution approximations. We demonstrate the importance of the re-initialization scheme in the following section.

6.4 Comparison with Different Re-initializations

To demonstrate the efficacy of our suggested re-initialization, we also perform a history-independent re-initialization as described in [27]. Table 6.3 shows the different parameters of re-initialization between the two schemes. In Figure 6.4a, we provide a comparison of the W_2 distance between the control and approximated distributions over time for the two different approximation schemes, and in Figure 6.4b, we perform PCA to visualize how well the approximations track the trajectory of the control evolution (see Section 5 for more detail).

The first Euler step shows similar results between the two experiments, but the history-independent scheme becomes (qualitatively good but) “relatively” inaccurate by the end of the first burn-in period. This is because the history-independent method re-initializes the microscopic properties with a “fixed” value regardless of current conditions, resulting in a large burn-in time to reach

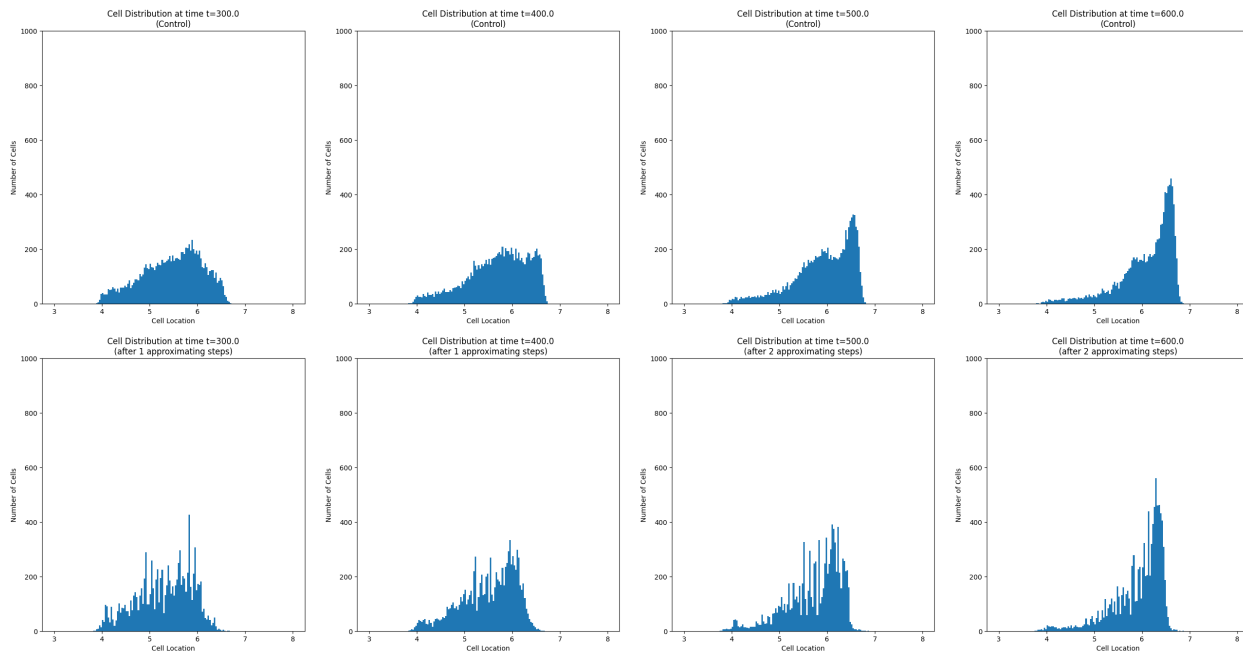


Figure 6.2: Histograms of bacteria locations after first two Euler steps (bottom) compared with corresponding times from control simulation (top). We run the micro-scale simulation until $t = 200$ (not pictured), take an Euler step to $t = 300$ (leftmost), burn in until $t = 400$ (second from left), take an Euler step to $t = 500$ (second from right), and burn in until $t = 600$ (rightmost).

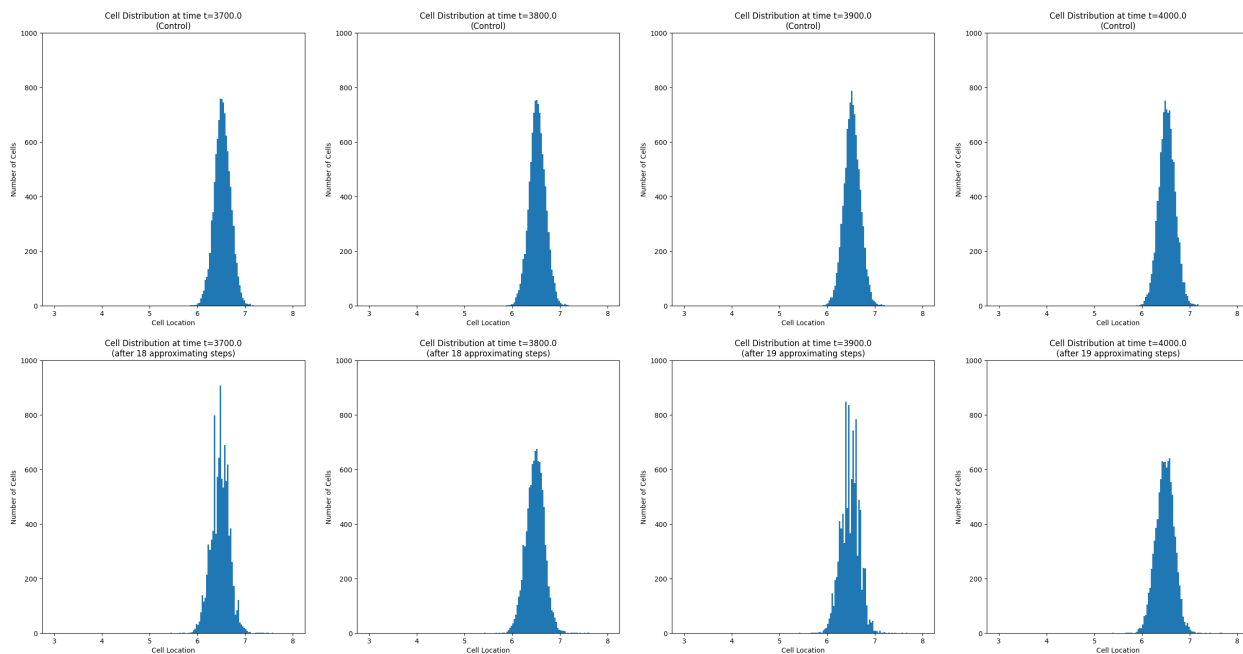
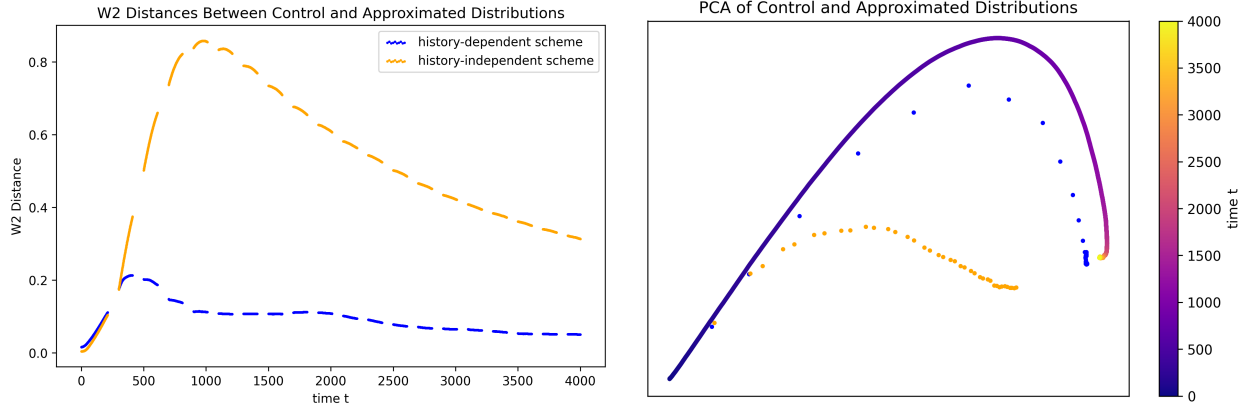


Figure 6.3: Histograms of bacteria locations after final two Euler steps (bottom) compared with corresponding times from control simulation (top). We take an Euler step from $t = 3600$ (not pictured) to $t = 3700$ (leftmost), burn in until $t = 3800$ (second from left), take an Euler step to $t = 3900$ (second from right), and finally burn in until $t = 4000$ (right-most), the end time.



(a) 2-Wasserstein distance between control distribution and approximated distributions versus time

(b) Projections of distributions onto the two principal components of the control distribution's evolution over time. The solid rainbow curve shows the control distribution, where the color represents time according to the color bar at the right. The blue and orange dots represent the approximations using the two re-initialization schemes.

Figure 6.4: Comparisons between control distributions and approximations

slow dynamics, while the history-dependent scheme uses the current microscopic properties to re-initialize after the next Euler step. In other words, the underlying variables (particularly u_2 and the flagella rotating direction) could not respond quickly enough to the fixed re-initialization. Furthermore, even though the distributions look the same after the first Euler step, the two methods still yield different subsequent microscopic behavior, leading to slightly different slow dynamics.

The observation in Figure 6.4a suggests that the underlying microscopic properties are important components in the micro-scale simulation. Hence, different settings of the properties result in different overall distribution behavior. In the language of Section 3, the tangent field that describes the distribution's evolution is somehow a function of these variables, not merely a function of position, so the method we choose to predict them across Euler steps is critical to our capability to approximate the evolution using optimal transport maps.

We demonstrate that both schemes show convergence to the control simulation within reasonable error bounds. This observation shows that different re-initializations of microscopic properties can change slow dynamics, and some schemes work better for particular problems. Here, the history-dependent scheme, which retains the flagella states from the previous step, better allows the distribution to continue moving at the same speed. In this experiment, since we used the Gaussian distribution of chemoattractant, which has a smooth change of its derivative, the change of rotating direction over time is not a normal event. Hence, keeping the same states provides us with better initialization. For the same reason, imposing the Euler forward step of u_2 may guarantee that the approximation is near the controlled simulation.

Like all mathematical models, choices about which prediction methods should be used depend entirely on the needs of the particular application. Unfortunately, these choices are mostly ad hoc and context-specific, so there is little to say in general about how they impact the accuracy of the overall approximation algorithm.

Acknowledgements. E. A. Nikitopoulos acknowledges support from NSF grant DGE 2038238. The work of I. G. Kevrekidis was partially supported by the US Department of Energy. A. Cloninger acknowledges support from NSF grants DMS 2012266 and CISE CCF 2403452.

References

- [1] Luigi Ambrosio and Nicola Gigli, *A user's guide to optimal transport*, Modelling and Optimization of Flows on Networks: Cetraro, Italy 2009 (Benedetto Piccoli and Michel Rascle, eds.), Lecture Notes in Mathematics, vol. 2062, Springer, Berlin, Heidelberg, 2013, pp. 1–155.
- [2] Luigi Ambrosio, Nicola Gigli, and Giuseppe Savaré, *Gradient flows in metric spaces and in the space of probability measures*, 2nd ed., Lectures in Mathematics. ETH Zürich, Birkhäuser, Basel, 2008.
- [3] Yann Brenier, *Polar factorization and monotone rearrangement of vector-valued functions*, Communications on Pure and Applied Mathematics **44** (1991), no. 4, 375–417.
- [4] Alexander Cloninger, Keaton Hamm, Varun Khurana, and Caroline Moosmüller, *Linearized Wasserstein dimensionality reduction with approximation guarantees*, Applied and Computational Harmonic Analysis **74** (2025), 101718.
- [5] Weinan E and Bjorn Engquist, *The heterogeneous multiscale methods*, Communications in Mathematical Sciences **1** (2003), no. 1, 87–132.
- [6] Weinan E, Di Liu, and Eric Vanden-Eijnden, *Analysis of multiscale methods for stochastic differential equations*, Communications on Pure and Applied Mathematics **58** (2005), no. 11, 1544–1585.
- [7] C. W. Gear, D. Givon, and I. G. Kevrekidis, *Virtual slow manifolds: The fast stochastic case*, AIP Conference Proceedings **1168** (2009), no. 1, 17–20.
- [8] C. W. Gear and Ioannis G. Kevrekidis, *Projective methods for stiff differential equations: Problems with gaps in their eigenvalue spectrum*, SIAM Journal on Scientific Computing **24** (2003), no. 4, 1091–1106.
- [9] C.W Gear and Ioannis G Kevrekidis, *Telescopic projective methods for parabolic differential equations*, Journal of Computational Physics **187** (2003), no. 1, 95–109.
- [10] C.W. Gear, Ioannis G. Kevrekidis, and Constantinos Theodoropoulos, *'Coarse' integration/bifurcation analysis via microscopic simulators: micro-Galerkin methods*, Computers & Chemical Engineering **26** (2002), no. 7–8, 941–963.
- [11] Nicola Gigli, *On Hölder continuity-in-time of the optimal transport map towards measures along a curve*, Proceedings of the Edinburgh Mathematical Society **54** (2011), no. 2, 401–409.
- [12] Somdatta Goswami, Aniruddha Bora, Yue Yu, and George Em Karniadakis, *Physics-informed deep neural operator networks*, Machine Learning in Modeling and Simulation: Methods and Applications (Timon Rabczuk and Klaus-Jürgen Bathe, eds.), Computational Methods in Engineering & the Sciences, Springer, Cham, 2023, pp. 219–254.

- [13] Somdatta Goswami, Katiana Kontolati, Michael D. Shields, and George Em Karniadakis, *Deep transfer operator learning for partial differential equations under conditional shift*, Nature Machine Intelligence **4** (2022), no. 12, 1155–1164.
- [14] Guillaume Hugué, D.S. Magruder, Alexander Tong, Oluwadamilola Fasina, Manik Kuchroo, Guy Wolf, and Smita Krishnaswamy, *Manifold interpolating optimal-transport flows for trajectory inference*, Advances in Neural Information Processing Systems **35** (2022), 29705–29718.
- [15] Ioannis G. Kevrekidis, C. William Gear, and Gerhard Hummer, *Equation-free: The computer-aided analysis of complex multiscale systems*, AIChE Journal **50** (2004), no. 7, 1346–1355.
- [16] Ioannis G. Kevrekidis, C. William Gear, James M. Hyman, Panagiotis G. Kevrekidis, Olof Runborg, and Constantinos Theodoropoulos, *Equation-free, coarse-grained multiscale computation: Enabling microscopic simulators to perform system-level analysis*, Communications in Mathematical Sciences **1** (2003), no. 4, 715–762.
- [17] Nikola B. Kovachki, Samuel Lanthaler, and Hrushikesh Mhaskar, *Data complexity estimates for operator learning*, preprint, arXiv:2405.15992 [cs.LG], 2024.
- [18] Seungjoon Lee, Yorgos M. Psarellis, Constantinos I. Siettos, and Ioannis G. Kevrekidis, *Learning black- and gray-box chemotactic PDEs/closures from agent based Monte Carlo simulation data*, Journal of Mathematical Biology **87** (2023), no. 1, 15.
- [19] John Lott, *Some geometric calculations on Wasserstein space*, Communications in Mathematical Physics **277** (2008), 423–437.
- [20] Lu Lu, Pengzhan Jin, Guofei Pang, Zhongqiang Zhang, and George Em Karniadakis, *Learning nonlinear operators via DeepONet based on the universal approximation theorem of operators*, Nature machine intelligence **3** (2021), 218–229.
- [21] Quentin Mérigot, Alex Delalande, and Frédéric Chazal, *Quantitative stability of optimal transport maps and linearization of the 2-Wasserstein space*, Proceedings of the Twenty Third International Conference on Artificial Intelligence and Statistics (Silvia Chiappa and Roberto Calandra, eds.), Proceedings of Machine Learning Research, vol. 108, PMLR, 2020, pp. 3186–3196.
- [22] H.N. Mhaskar, *Local approximation of operators*, Applied and Computational Harmonic Analysis **64** (2023), 194–228.
- [23] Caroline Moosmüller and Alexander Cloninger, *Linear optimal transport embedding: Provable Wasserstein classification for certain rigid transformations and perturbations*, Information and Inference: A Journal of the IMA **12** (2023), no. 1, 363–389.
- [24] Felix Otto, *The geometry of dissipative evolution equations: The porous medium equation*, Communications in Partial Differential Equations **26** (2001), no. 1–2, 101–174.
- [25] Gabriel Peyré and Marco Cuturi, *Computational optimal transport*, Foundations and Trends in Machine Learning **11** (2019), no. 5–6, 355–607.
- [26] Filippo Santambrogio, *Optimal transport for applied mathematicians: Calculus of variations, PDEs, and modeling*, Progress in Nonlinear Differential Equations and Their Applications, vol. 87, Birkhäuser, 2015.

- [27] S. Setayeshgar, C. W. Gear, H. G. Othmer, and I. G. Kevrekidis, *Application of coarse integration to bacterial chemotaxis*, *Multiscale Modeling & Simulation* **4** (2005), no. 1, 307–327.
- [28] Alexander Tong, Jessie Huang, Guy Wolf, David van Dijk, and Smita Krishnaswamy, *TrajectoryNet: A dynamic optimal transport network for modeling cellular dynamics*, *Proceedings of machine learning research* **119** (2020), 9526–9536.
- [29] Eric Vanden-Eijnden, *Numerical techniques for multi-scale dynamical systems with stochastic effects*, *Communications in Mathematical Sciences* **1** (2003), no. 2, 385–391.
- [30] Wei Wang, Dejan Slepčev, Saurav Basu, John A. Ozolek, and Gustavo K. Rohde, *A linear optimal transportation framework for quantifying and visualizing variations in sets of images*, *International Journal of Computer Vision* **101** (2013), 254–269.
- [31] Yewei Xu and Qin Li, *Forward-Euler time-discretization for Wasserstein gradient flows can be wrong*, preprint, arXiv:2406.08209 [stat.ML], 2024.